Characterization of Carbon Dioxide on Icy Moons: Laboratory Ice Analogues and JWST Observations

Léon Schiltz

Delft University of Technology

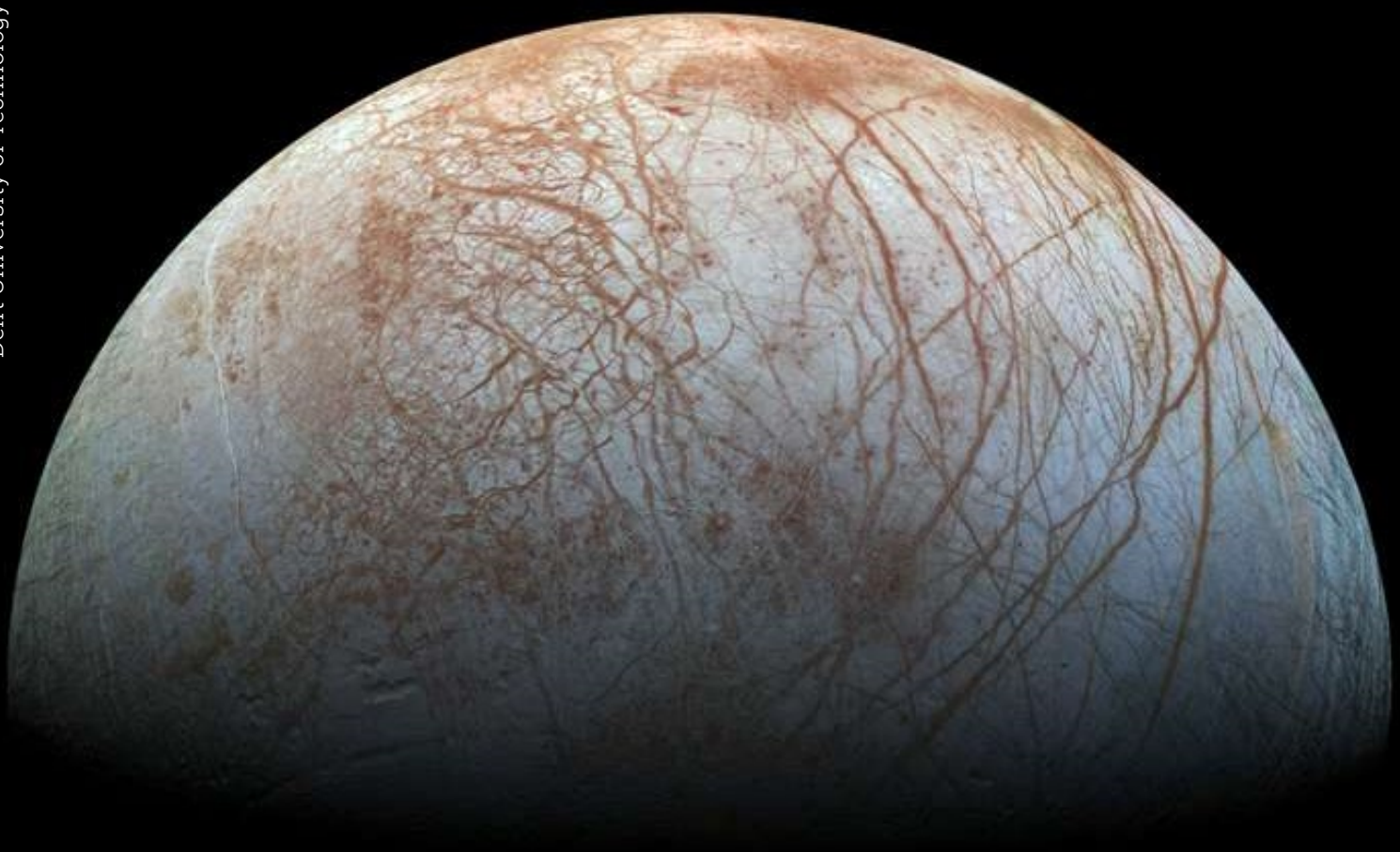

TU Delft

Characterization of Carbon Dioxide on Icy Moons: Laboratory Ice Analogues and JWST Observations

by

Léon Schiltz

to obtain the degree of Master of Science
at the Delft University of Technology,
to be defended publicly on Friday December 1, 2023.

Student number:	4680863	
Project duration:	March 20, 2023 – December 1, 2023	
Thesis committee:	Dr. S. M. Cazaux	TU Delft, Supervisor
	Dr. G. M. Muñoz Caro	CAB, Supervisor
	Dr. A. Cervone	TU Delft, Chair
	Dr. S. J. M. Potin	TU Delft, Examiner

Cover: NASA/JPL-Caltech

An electronic version of this thesis is available at http://repository.tudelft.nl/.

TU Delft

Acknowledgements

I extend my deepest gratitude to several individuals whose support and guidance were instrumental in the completion of this thesis.

First and foremost, I am profoundly indebted to my daily supervisors, Stéphanie Cazaux and Guillermo Muñoz Caro. Their shared expertise, thoughtful feedback, and constant encouragement served as a compass, steering this thesis towards excellence. Beyond their professional guidance, their approachability and willingness to engage in thorough discussions were instrumental in overcoming challenges and fostering a dynamic academic environment. I am deeply grateful for the patience, encouragement, and the time they dedicated to nurturing my growth as a researcher.

I also wish to express my sincere appreciation to my colleagues at CAB, whose collective knowledge, insightful discussions, and collaborative spirit greatly enriched my academic journey. The exchange of ideas and shared experiences within this remarkable community has played an integral role in the development of this thesis. Their diverse perspectives and willingness to engage in constructive debates significantly contributed to the refinement and evolution of my research.

Furthermore, my heartfelt gratitude goes out to my friends and family for their unwavering support, understanding, and encouragement during this challenging yet rewarding phase of my academic pursuit. Their unconditional love and belief in my abilities have been my pillar of strength, enabling me to navigate through obstacles and celebrate successes.

The combined contributions of my supervisors, colleagues, friends, and family have been indispensable in the completion of this thesis. I am profoundly thankful for their unwavering support, guidance, and encouragement throughout this academic endeavor.

Léon Schiltz
Delft, December 2023

Abstract

Mixed ices of CO_2 and water, prevalent in cometary nuclei, solar system satellites, and interstellar dust particles, have posed a persistent challenge in understanding the fundamental behaviors of carbon dioxide (CO_2) in these icy environments. Specifically, the intriguing shift in the CO_2 stretching fundamental band observed on icy moons like Europa and Ganymede has remained enigmatic. In this study, we undertake a comprehensive investigation to elucidate this phenomenon by characterizing carbon dioxide on Ganymede through temperature-dependent spectral analyses.

Laboratory experiments involve the study of pure CO_2 ice and its mixtures with water at varying concentrations, mimicking astrophysical conditions. Utilizing temperature-programmed desorption (TPD) and Fourier-transform infrared spectroscopy (FTIR) techniques, coupled with Gaussian deconvolution of obtained spectra, we explore the molecular interactions underlying the observed spectral shifts. Our experiments at 10 K under ultra-high vacuum conditions replicate interstellar medium conditions, providing crucial insights into CO_2 behavior in icy environments.

In the discussion, a detailed overview is presented of the positions and behaviors of the fitted Gaussians for the asymmetric stretching bands of CO_2 in pure form and when co-deposited with water. The temperature-dependent evolution of these bands reveals intricate dynamics, emphasizing the influence of CO_2 concentration on the shifting positions and shapes of the spectral features.

The conclusions highlight key findings, including the complex nature of CO_2 interactions within water ice, manifested in the emergence of multiple peaks at different concentrations. The thermal desorption analyses unveil distinct desorption behaviors, shedding light on the interactions during ice phase transitions. Importantly, our laboratory results align with observations from the James Webb Space Telescope (JWST), providing a synergistic approach to understanding CO_2 behavior on icy worlds. The variations observed in Ganymede's spectra across latitudes and longitudes further corroborate the influence of temperature and UV irradiation on CO_2 dynamics within the ice.

This study contributes valuable insights into the molecular intricacies of CO_2 in mixed ices, bridging laboratory experiments with observational data. The synergy between these approaches promises a more profound understanding of CO_2 behavior in diverse astrophysical environments, advancing our knowledge of icy worlds in our Solar System and beyond.

Contents

List of Figures

Nomenclature

Abbreviations

CO_2	Carbon Dioxide
DFT	Density Function Theory
FITS	Flexible Image Transport System
FTIR	Fourier-Transform Infrared Spectroscopy
FWHM	Full Width at Half Maximum
H_2O_2	Hydrogen Peroxide
IFU	Integral Field Unit
IR	Infrared
JWST	James Webb Space Telescope
K	Kelvin
CH_3OH	Methanol
MIRI	Mid InfraRed Instrument
NIR	Near InfraRed
QMS	Quadrupole Mass Spectrometer
TPD	Temperature Programmed Desorption
UV	Ultra-violet
H_2O	Water

Symbols

N	Column Density
A	Band Strength
τ_ν	Optical Depth
$\mathrm{d}\nu$	Wavelength Differential
τ	Integrated Optical Depth
d	Ice Thickness
n_{ice}	Refractive Index Ice
λ	Wavelength
θ_t	Angle
t_{minima}	Time between two minima
dr_{avg}	Average Deposition Rate
a	Amplitude
μ	Expected Peak Center
σ	Standard Deviation
δA	Error

1

Introduction

Icy moons in our Solar System, particularly Europa and Ganymede, have remained celestial enigmas, concealing beneath their icy exteriors the potential for profound scientific discoveries. These moons have long captivated the attention of astronomers, planetary scientists, and astrobiologists due to their intriguing characteristics, including the presence of subsurface oceans beneath their icy crusts (Carr et al. 1998). These vast bodies of water, like the global ocean hidden beneath Europa's surface, have sparked tantalizing speculation about the possibility of sustaining life beyond Earth.

Carbon dioxide (CO_2) mixed with water ice is known to be a significant component found on these moons (e.g. Grundy et al. 2003; Buratti 2005), alongside its presence in comets' frozen nuclei (Crovisier 2006a; Crovisier 2006b) and interstellar dust particles (e.g. Dartois et al. 2005; Draine 2003). The intriguing observation of the slight shift in the CO_2 stretching fundamental band on various Galilean satellites, notably to a shorter wavelength, has raised questions about its interaction with other surface materials. These phenomena serve as a puzzle awaiting resolution, and they form the basis for this research and experimentation.

Understanding the nature and behavior of compounds such as CO_2 within the ices of these moons is critical not only for unraveling their chemical composition but also for shedding light on the geophysical processes at play in these unique extraterrestrial environments. Moreover, the intricate interplay between various compounds, including the behavior of CO_2 within these ices, holds essential clues about the history, evolution, and potential habitability of these celestial bodies.

The quest to unravel the mysteries of these icy worlds is not merely a scientific endeavor; it is a journey that could redefine our understanding of planetary formation, the potential for life beyond Earth, and the broader implications for habitability in the cosmos. Space missions such as the Galileo spacecraft, which provided vital data and images of these moons, have paved the way for further exploration, igniting a fervent interest in their composition and habitable potential. Additionally, upcoming missions like the Europa Clipper aim to conduct detailed reconnaissance and explore the possibility of sustaining life on these celestial bodies.

To comprehend the peculiarities of CO_2 behavior within the ices on these moons, extensive research employing laboratory simulations has been undertaken. Solid H_2O/CO_2 ice mixtures, as laboratory analogues of astrophysical objects, have been studied for many years, mainly by infrared spectroscopy and mass spectrometry, in temperature programmed desorption (TPD) experiments (see e.g. Sandford and Allamandola 1990; Ehrenfreund 1997b; Bernstein et al. 2005; Kumi et al. 2006; Malyk et al. 2007). From these studies, the interaction between CO_2 and H_2O on a molecular level has been shown to cause significant changes in the position and profile of CO_2 peaks in the IR. However, a concise answer to why the CO_2 stretching fundamental band on icy moons, like Europa and Ganymede, shifts remains elusive. Also, the assignment of the different bands to ice structure is still missing in current literature.

In this research, experiments are conducted under conditions mimicking the interstellar medium, involving temperature studies on CO_2 ice, both in its pure form and in co-deposition with varying ratios of water. Through techniques such as temperature programmed desorption (TPD) and Fourier-transform

infrared spectroscopy (FTIR), the spectral properties are analyzed. The utilization of deconvolution techniques, particularly Gaussian distributions, has proven instrumental in deciphering the complex spectral data acquired, shedding light on the behavior of CO_2 when combined with water ice.

The combination of laboratory-generated spectra with observations from space-based platforms like the James Webb Space Telescope (JWST) strengthens the comprehensive approach to resolving the enigma of CO_2 behavior on these icy moons. This synergistic approach promises to offer a deep understanding of the fundamental properties of CO_2 ice under various conditions and environments.

The relevance of this multifaceted research extends beyond the realms of planetary science. It extends into broader scientific inquiries, encompassing the search for life beyond Earth, the origins of life, and the potential habitability of exoplanets. By studying the behavior of compounds such as CO_2 within the ices of these celestial bodies, researchers aim not only to unlock the secrets of planetary evolution but also to contribute to the greater pursuit of understanding our place in the vast cosmos.

1.1. Research Questions

According to what has been explored in the introduction, there is still missing information on icy moons, their spectral features for carbon dioxide and what this means for the ice structure. Therefore, the goal of the MSc thesis is to characterize the carbon dioxide on icy moons by comparing laboratory ice analogues and JWST observations. As a result, the main research question is as follows:

"Which features in infrared spectra obtained from JWST observations contribute to our understanding of the characteristics of ices and surface features of icy moons?"

Several sub questions are developed to solve the aforementioned research questions.

1: What specific spectral features in the infrared range are indicative of certain types of ices and surface features on icy moons?
2: How can these characteristics be attained through laboratory experiments?
3: What is the desorption pattern of CO_2:H_2O mixtures? And what effect does the heating ramp have on the desorption peaks?
4: What effect does the abundance of CO_2 in water ice have on the asymmetric stretching band?
5: How do laboratory spectra relate to JWST observations?

1.2. Report Outline

This report starts with a brief introduction on scientific background given in Chapter 2. This thesis' research and findings have been published in the form of a scientific journal paper, which is contained in Chapter 3. Chapter 4 contains the results and recommendations for further study.

2

Scientific Background

This chapter will provide a quick review of the scientific information required to comprehend the scientific paper. This will be accomplished by presenting the principle of spectroscopy, namely gas versus ice. An outline of prior carbon dioxide laboratory research will also be provided. Finally, recent JWST discoveries for Ganymede and Europa will be presented.

2.1. Spectroscopy

Infrared spectroscopy is a powerful analytical technique that exploits the interaction between matter and infrared radiation. It is widely utilized in various scientific fields, including chemistry, biochemistry, and environmental science. The fundamental principle of infrared spectroscopy lies in the fact that molecules absorb specific frequencies of infrared light, leading to vibrational transitions that provide valuable information about the molecular composition and structure of a substance. The basic fundamentals of infrared spectroscopy involve the measurement of the absorption of infrared radiation by chemical bonds within a sample. Molecules have characteristic vibrational modes associated with their bonds, and when infrared radiation matches the energy required to excite these vibrations, absorption occurs. The resulting infrared spectrum provides a unique fingerprint for each molecule, allowing for the identification of functional groups and structural features.

Gas-phase infrared spectroscopy is particularly valuable for the analysis of gaseous substances. In the gas phase, molecules have greater freedom of movement, leading to well-defined and sharp absorption peaks in the spectrum. This enables precise identification of individual molecular species and determination of their concentrations. Gas-phase infrared spectroscopy is commonly employed in environmental monitoring, industrial processes, and atmospheric studies to detect and quantify trace gases. In contrast, ice spectroscopy using infrared techniques is crucial for the study of frozen environments, both on Earth and in extraterrestrial settings. Ice spectra reveal information about the composition of frozen materials, providing insights into the conditions and processes that shaped these environments. Infrared spectroscopy is particularly useful in identifying molecular constituents in icy samples, such as water ice, carbon dioxide, and methane, often found in celestial bodies like icy moons and comets.

When comparing gas and ice spectroscopy in the infrared region, notable distinctions arise from the different properties of these phases. In gas-phase spectroscopy, the emphasis is on the identification of isolated gas molecules with well-defined absorption peaks. In ice spectroscopy, the focus shifts to understanding the interactions and mixtures of molecules within a frozen matrix. The broader and sometimes overlapping absorption bands in ice spectra can present challenges in precisely identifying individual components.

In summary, infrared spectroscopy serves as a versatile tool for the analysis of molecular composition and structure. Gas-phase infrared spectroscopy is adept at identifying and quantifying gases, while ice spectroscopy extends the application to frozen environments, shedding light on the composition of ices and their significance in planetary and environmental studies. These complementary approaches con-

tribute significantly to our understanding of the diverse molecular landscapes within gases and frozen materials.

2.2. Laboratory Ice Spectra

CO_2 has five active bands in the mid-infrared (4000-400 cm^{-1}, 2.5-25 μm) (Figure 2.1). The focus for this research is on the $^{12}CO_2$ asymmetric stretching fundamental (ν_3). The most prominent CO_2 infrared band arises from the asymmetric stretching vibrations of the C=O bond and occurs around 2340 cm^{-1}. Typically, this band experiences a redshift of 2-8 cm^{-1} from its gas phase value (2348 cm^{-1}). This redshift may indicate one of two possibilities in these solids: (1) the trapping site is generally slightly larger than the CO_2 molecule, as more confined sites tend to induce blueshifts, or (2) a weak chemical complex forms wherein some of the bonding electrons of the CO_2 molecule become delocalized, resulting in a subtly weakened C=O bond (Sandford and Allamandola 1990). It was found that the position and width of the CO_2 asymmetric stretch band is temperature dependent. In general, the bands decrease in width as the temperature is increased. The CO_2 band generated by pure CO_2 ice holds significance for a couple of reasons. Firstly, it exhibits a wing on the high-frequency side that persists across most of the ice's thermal stability range (Sandford and Allamandola 1990). Secondly, at 10 K, it displays a robust shoulder on the low-frequency side of the main band. Notably, this shoulder experiences a rapid decrease in strength as the ice is warmed up (Sandford and Allamandola 1990). CO_2/H_2O combinations exhibit exceptional behavior, exerting a substantial influence on CO_2

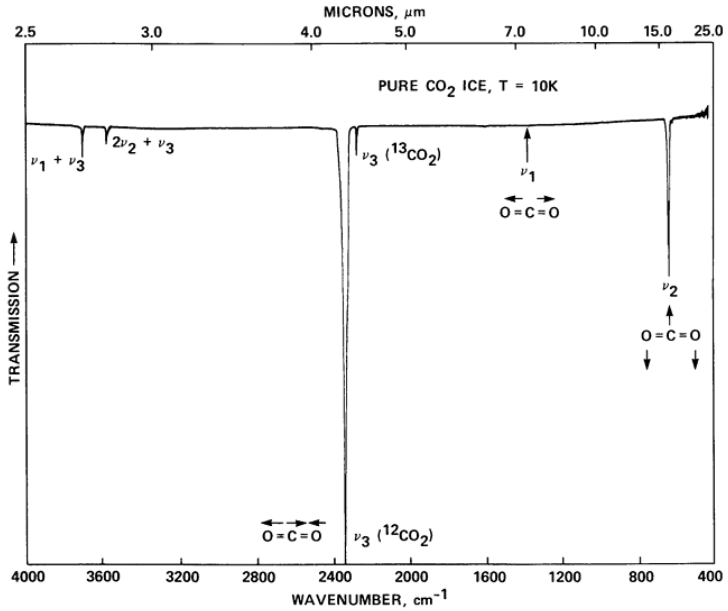

Figure 2.1: Spectrum of an amorphous pure CO_2 ice deposited and held at 10 K. Note the five bands for CO_2 (Sandford and Allamandola 1990).

band profiles—an essential factor in determining abundance and studying interstellar CO_2. Beyond a specific percentage of water ice in a CO_2/H_2O combination, the emergence of molecule aggregation and additional trapping sites leads to a distinct CO_2 stretching mode (Ehrenfreund 1997b). A second band emerges at 2328 cm^{-1}, causing a significant broadening of the band (FWHM = 30 cm^{-1}) and an asymmetric profile shifted by approximately 15 cm^{-1} to a lower frequency. Interestingly, even when CO_2 and H_2O concentrations are equal, this profile remains constant. In polar mixes where H_2O is more abundant in the ice matrix, the band position peaks at around 2341 cm^{-1}, similar to pure CO_2, with a reduced FWHM of 15 cm^{-1}. In mixes with CO_2:H_2O ratios of 10:1, 10:6, and 1:1, a consistent profile is observed, characterized by a broad band width (12 cm^{-1}) and a pronounced redshift.

2.3. JWST Discoveries

A recent paper, by Bockelée-Morvan et al. 2023, explores the composition and thermal aspects of Ganymedes' surface, as well as the relationships and distribution of ice and non-water-ice elements. It was found that the 4.26 μm band of CO_2 exhibits variations in both band center and shape across latitudinal and regional scales in both hemispheres. These variations suggest the presence of CO_2 in diverse physical states on the surface. Notably, the characteristics of the band center and shape show correlations with both the Bond albedo and the abundance of H_2O ice. In the polar regions abundant with ice and particularly exposed to Jupiter's plasma irradiation, the CO_2 band exhibits a noticeable red shift compared to other terrains. Moving to the boreal region of the leading hemisphere, the dominant component of the CO_2 band is characterized by a higher wavelength at approximately 4.27 μm, indicating the presence of CO_2 trapped in amorphous water ice. Coincidentally, amorphous water ice is observed in the same region. This suggests a potential interconnection between the formation and/or trapping of CO_2 and the formation and/or structure of amorphous water ice in this specific geographical area. Furthermore, at equatorial latitudes, particularly on dark terrains, the observed phenomena of band broadening and blue shift indicate the likely presence of CO_2 adsorbed or trapped on non-icy materials, such as minerals or salts (Bockelée-Morvan et al. 2023).

On Europa, the observed 4.25 μm absorption band attributed to $^{12}CO_2$ exhibits a distinctive double-peaked structure, in contrast to the single-peaked form characteristic of crystalline CO_2 ice (Villanueva et al. 2023). Notably, the best match to this double-peaked shape was identified in a laboratory spectrum of a mixture consisting of CO_2, H_2O, and CH_3OH in a ratio of 1:0.8:0.9, respectively, measured at a temperature of 114 K. The temperature of this laboratory spectrum aligns with the range previously recorded for different hemispheres of Europa, spanning from 90 to 130 K.

This observation suggests the potential storage of CO_2 within a matrix rich in water and organic compounds on Europa. Intriguingly, despite this indication, our spectra did not reveal any bands associated with CH_3OH ice or other organic molecules. The significance of this finding warrants further investigation and consideration in the broader context of Europa's complex surface composition.

Hydrogen peroxide (H_2O_2) has been identified across Ganymede's surface, with a notably higher concentration in the polar regions, where water ice is most abundant (Trumbo et al. 2023). This distribution aligns with H_2O_2 being a byproduct of water ice radiolysis, particularly enhanced in the open field line regions (Trumbo et al. 2023). However, a noteworthy observation is the lack of strong correlation between the maps of H_2O_2 and carbon dioxide (CO_2) (Trumbo et al. 2023; Bockelée-Morvan et al. 2023), suggesting that the abundance of CO_2 is unlikely to exert a significant influence on H_2O_2 production. Furthermore, the investigation into the red-shifted component of the band, associated with CO_2 in conjunction with water ice, reveals an enrichment of CO_2 in the polar regions of the leading hemisphere, akin to the distribution of H_2O_2. Despite this similarity, there is no precise pixel-to-pixel correspondence between the specific locations of both species (Trumbo et al. 2023). The distinct mapping patterns imply that while CO_2 and H_2O_2 share some environmental factors, their production and distribution are not entirely governed by the same processes on Ganymede's surface.

In contrast to Europa, where hydrogen peroxide (H_2O_2) exhibits increased abundance in the most ice-poor and warmest regions, the distribution of H_2O_2 on Ganymede follows a different pattern, with heightened abundance observed in the most ice-rich and coldest regions (Trumbo et al. 2023). This discrepancy in H_2O_2 distribution between the two moons is highlighted in previous studies (Spencer et al. 1999; Trumbo et al. 2019). The enhanced levels of H_2O_2 on Europa's chaos terrains have led to hypotheses linking this phenomenon to the presence of carbon dioxide (CO_2) or other electron-accepting ice contaminants. These substances are thought to play a role in scavenging destructive electrons generated during the irradiation of the ice, thereby slowing down the degradation of H_2O_2 (Trumbo et al. 2019; Trumbo et al. 2023). This proposed mechanism suggests a complex interplay between ice composition and the radiation environment, influencing the distribution and preservation of H_2O_2 on these Jovian moons.

3

Scientific Article

The study described here has been recorded in the form of a scientific publication, which will be submitted to the journal Astronomy and Astrophysics (A&A). This chapter contains the article, which adheres to the standard A&A template and criteria.

Appendix A and Appendix B will not be included in the article. However, these appendices provide additional information on calculations, methods and software used in the article. Furthermore, extra experiments are elaborated upon and discussed.

Astronomy & Astrophysics manuscript no. output
November 17, 2023

Characterization of Carbon Dioxide on Icy Moons: Laboratory Ice Analogues and JWST Observations

L. Schiltz[1]

Faculty of Aerospace Engineering, Delft University of Technology, Delft, The Netherlands
e-mail: leon.schiltz@hotmail.com

Received XXXXXX; accepted XXXX

ABSTRACT

Context. Icy moons are celestial bodies characterized by frozen surfaces primarily composed of water ice, with some containing a variety of other compounds, including carbon dioxide.
Aims. Investigate the cause of the observed shift in the CO_2 stretching fundamental band on icy moons like Ganymede. Explore the spectral behavior of CO_2 ice concerning temperature and varied H_2O:CO_2 deposition ratios.
Methods. Analyzed pure CO_2 ice and ice mixtures with different CO_2 concentrations using FTIR spectroscopy and TPD experiments at 10 K under ultra high vacuum conditions. Applied Gaussian deconvolution to understand spectral changes and temperature-related characteristics. Comparing lab spectra to JWST observation of Ganymede's leading hemisphere.
Results. Pure CO_2 ice exhibited temperature-driven spectral shifts and demonstrated a desorption peak at 85 K. Varying CO_2 concentrations in ice mixtures caused distinct spectral changes and desorption behaviors at different temperatures, illuminating intricate CO_2 and H_2O interactions. Moreover, the number of discernible peaks increased from two in pure CO_2 to three in CO_2-water mixtures, influencing the assignment of band locations.
Conclusions. The investigation of pure CO_2 ice spectra showcased distinct redshifts and changes in peak shape, emphasizing its temperature-dependent evolution from 10 K to 80 K. CO_2 mixed with water ice (low and high concentration) exhibits multiple peaks, of which two are the same as for pure CO_2. The different CO_2 bands are assigned as follows: $\tilde{\nu_{3,1}}$ is assigned to CO_2 dangling bonds in which CO_2 molecules are found in pores or cracks, $\tilde{\nu_{3,2}}$ is due to several CO_2 molecules trapped in the ice (segregated) and $\tilde{\nu_{3,3}}$ is CO_2 interacting with water ice, which means embedded in the water ice. JWST NIRSPEC spectra reveal latitudinal variations in CO_2 bands on Ganymede, with $\tilde{\nu_{3,1}}$ dominant in colder regions and $\tilde{\nu_{3,3}}$ prevalent in equatorial latitudes. Gaussian fits confirm distinct CO_2 states shifting with temperature, indicating CO_2 embedding in water ice in polar regions. Examining longitudinal spectra reveals fluctuations in CO_2 spectra throughout the day. The observed blueshift of the $\tilde{\nu_{3,1}}$ peak at 2351 cm^{-1} is associated with ice porosity, while shifts in limb spectra are attributed to the influences of UV irradiation and temperature variations.

Key words. Carbon dioxide ices – methods: laboratory – JWST observations – infrared spectroscopy – icy moons

1. Introduction

Mixed ices of CO_2 and water are known to be present, for example, in the frozen nuclei of comets (Crovisier (2006a,b)), in various satellites of our Solar System (e.g. Grundy (2003); Buratti (2005)), and as components of dust interstellar particles (e.g. Dartois (2005); Draine (2003)). On several Galilean satellites, the CO_2 stretching fundamental band, which is ordinarily at 4.27 μm, is displaced slightly to a shorter wavelength (4.26 μm) and is thought to come from CO_2 that has been complexed in some way with other surface materials. Prompted by these findings, solid H_2O/CO_2 ice mixtures, as laboratory analogues of astrophysical objects, have been studied for many years, mainly by infrared spectroscopy and mass spectrometry, in temperature programmed desorption (TPD) experiments (see e.g. Sandford and Allamandola (1990); Ehrenfreund (1997); Bernstein (2005); Kumi (2006); Malyk (2007)). From these studies, the interaction between CO_2 and H_2O on a molecular level has been shown to cause significant changes in the position and profile of CO_2 peaks in the IR. However, a concise answer to why the CO_2 stretching fundamental band on icy moons, like Europa and Ganymede, shifts remains elusive.

In the present work, an attempt is made to find an explanation for this shift by characterizing the carbon dioxide on Europa and Ganymede. This is achieved by investigating the influence of temperature on the spectral properties of CO_2 ice, and in particular the behavior of the CO_2 stretching mode which in its pure form peaks around 4.266 μm (2344 cm^{-1}). CO_2 is first studied in its pure form, and afterwards co-deposited with water so that the H_2O:CO_2 deposition ratio is varied. In particular, a low (<5%) and high (>25%) carbon dioxide concentration in the ice are worked with. Experiments are carried out at 10 K and ultra high vacuum conditions to mimic the conditions in the interstellar medium. This research uses a combination of the following two techniques, TPD and FTIR, on a variety of experimental conditions. Additionally, the spectra obtained from the experiment are deconvoluted using Gaussian distributions. This technique is first applied to pure CO_2 ice and afterwards for the mixtures. It was found that the asymmetric stretching band ν_3 of pure CO_2 can be deconvoluted in two Gaussian distributions, and three when mixed with water. The evolution of the integrated absorbance areas, band shape and position as a function of temperature can be compared to the TPD curve in order to assign the bands to different molecular interactions, and thus characterizing the type of CO_2 ice. The synergy between laboratory studies and data gathered by the James Webb Space

Telescope (JWST) enriches our comprehensive approach to understanding CO_2 behavior on ice worlds. This combination promises a thorough exploration of the fundamental properties of CO_2 ice in various conditions.

The paper's structure is organized as follows: Section 2 outlines the experimental setup and the determination of the gas mixture ratio. Section 3 focuses on the spectroscopic behavior of pure CO_2 ice, elucidating the ν_3 stretching band's shape and location alongside the TPD curve. Section 4 and Section 5 exhibit the acquired laboratory spectra for low and high CO_2 concentrations in water ice as a function of temperature, accompanied by explanations of integrated absorbance areas and TPD curves. Finally, Section 7 delves into the application of findings to icy moons, specifically Europa and Ganymede, involving a comparison of new experimental results with observations.

2. Experimental Method

2.1. ISAC Setup

The experiments reported in this work have been performed with the Interstellar Astrochemistry Chamber (ISAC), described in more detail in Muñoz Caro (2010). ISAC is an ultra-high vacuum (UHV) chamber with a base pressure of 4×10^{-11} mbar designed to simulate the conditions present in the interstellar medium (ISM), regarding temperature, pressure and ultraviolet (UV) radiation field. A closed-cycle He cryostat allows to cool down the tip of the cold finger to 8 K, where a sample holder with a Potassium Bromide (KBr) window acting as the substrate for ice deposition is located. A schematic representation is shown in Figure 1. A Lakeshore temperature controller 331 with 0.1 K accuracy controls the temperature. The gas line, which permits the introduction of gas species with regulated compositions, is linked to the main chamber through a leak valve. The identification of the species present in the chamber is done via a quadrupole mass spectrometer (QMS, Pfeiffer Vacuum, Prisma QMS 200). The valve is opened during deposition, and the gas is delivered to the cold substrate through a deposition tube. This tube's end is roughly placed at a distance of 3 cm from the substrate. Fourier-transform infrared spectroscopy (FTIR) in transmittance mode using a Bruker Vertex 70 at a working spectral resolution of 2 cm^{-1} is used to record infrared spectra during deposition, and temperature programmed desorption (TPD) using a heating ramp in K/min. ISAC uses laser interferometry at 632.8 nm to assess changes in ice thickness (Gonzalez Díaz (2022)). A 5.0 mW He-Ne red laser and a Silicon Photodiode Power Sensor to measure the optical power of the laser light (model S120C) are mounted at an angle of 6°, as seen in Figure 1.

When the deposition temperature of 10 K is attained, the experiment begins. Then, by opening the leak valve of gas line 2 in Figure 1, a mixture of H_2O and CO_2 is fed into the main chamber, and a deposition pressure of $2{\times}10^{-7}$ mbar is achieved. To investigate the influence of deposition temperature and pressure on the spectral properties of CO_2 ice, and in particular the behavior of the CO_2 stretching mode, experiments are carried out at 70 K and higher pressures (see Appendix B). First, CO_2 is studied in its pure form, and afterwards co-deposited with varying H_2O:CO_2 deposition ratio. During the deposition of the gas mixture to form the ice, infrared spectra at 45° incidence of the beam relative to the substrate were collected every 300 s. Warming up the samples after deposition was done at 0.2 K min^{-1} until a temperature of 210 K was attained, ensuring that both the CO_2 and H_2O were entirely desorbed and that the chamber had no residues. IR measurements were done every 300 s again, yielding a spectrum every 1 K increment.

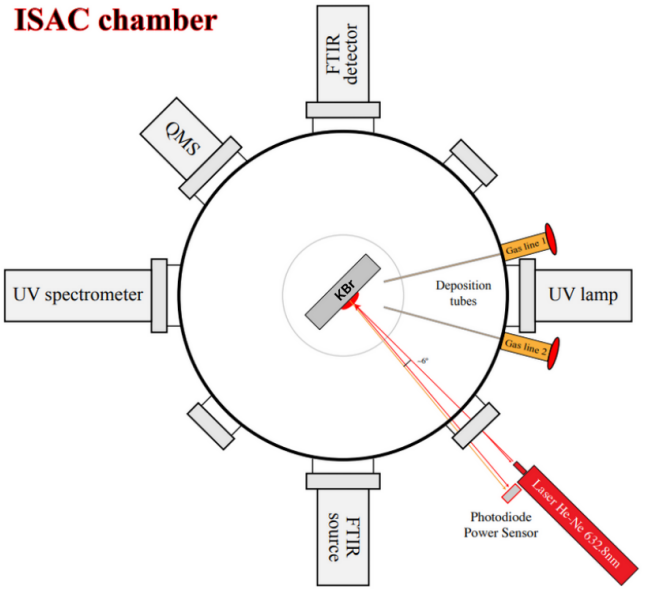

Fig. 1. ISAC intersection at the ice sample level. The many measuring components and sensors, including the laser, are displayed. The FTIR source is positioned on one side and the FTIR detector on the other. The UV spectrometer is placed directly across from the vacuum-UV lamp, see Gonzalez Díaz (2022) for more details.

The key parameters measured during the experiments using various devices are the laser intensity to measure the ice thickness (see Appendix A.2.), pressure inside the chamber, the ion currents of the relevant molecules (via QMS) and the temperature. The temperature of the ice sample was measured using a silicon diode sensor connected to the sample holder and placed directly below the ice sample. A Bayard-Alpert gauge positioned about 23 cm below the plane where deposition occurs was used to measure the pressure in the main chamber of ISAC. Laser interference was monitored continually, resulting in an interference pattern during ice deposition and a new interference pattern during TPD. The ice column density was calculated using IR spectroscopy and the areas acquired by integrating the absorption bands. This will be covered in more detail in the following subsection.

2.2. Estimation gas mixture ratio

The integration of the infrared absorption band yields the column density N of the ice layer accreted on the cold substrate in molecules cm^{-2} with the following formula:

$$N = \int_{band} \frac{\tau_\nu d\nu}{A} \tag{1}$$

with A the band strength in cm $molecules^{-1}$, τ_ν the optical depth of the band and dν the wavenumber differential in cm^{-1}. The integrated absorbance is equal to $0.43 \times \tau$, where τ is the integrated optical depth of the band. The gas mixture ratio is calculated by dividing the column density of the carbon dioxide anti-symmetric stretching band to the water stretching band. For both molecules, the band strength of the pure ices at 10 K are used, resulting in the H_2O band set to $2.0{\times}10^{-16}$ cm $molecules^{-1}$ (Hagen (1981)). The band strength for the pure CO_2 anti-symmetric stretching band equals $7.6{\times}10^{-17}$ cm $molecules^{-1}$ (Bouilloud

(2015)). For the ices with a very low percentage of CO_2, the error for estimating the mixture ratio is negligible when using the band strength for pure ices instead of mixed ices. Additionally, up to a CO_2 concentration of 25 % in the ice, the band strengths for the mixture are very close to the values for pure ices, resulting in an error less than 5% (see Appendix A.1.). To compute the integrated intensities of the H_2O stretching peaks, the measured peak positions and the integration bounds in $cm^{-1}(\mu m)$ are taken between a lower bound of 3000 (3.33) to an upper bound of 3600 (2.78). The same method is applied to the CO_2 anti-symmetric stretching mode with lower bound 2330 (4.29) and upper bound 2360 (4.24). A summarizing table of the experimental parameters can be found in Table 1, where p_{dep} is the total pressure in the ISAC chamber during deposition of the ice, T_{dep} is the temperature at which the ice is deposited, d_{ice} is the ice thickness and dT/dt is the heating rate in Kelvin per minute.

Table 1. Experimental Parameters

Composition	p_{dep} (mbar)	T_{dep} (K)	d_{ice} (μm)	$\frac{dT}{dt}$ (K/min)
Pure CO_2	2×10^{-7}	10	0.62	0.5
$1H_2O$:0.04CO_2	2×10^{-7}	10	0.54	0.2
$1H_2O$:0.25CO_2	2×10^{-7}	10	0.67	0.2

3. Pure CO_2 ice

Pure CO_2 ice has been deposited at 10 K and warmed up until 100 K. The characteristics of the CO_2 ice stretching band at 2345 cm^{-1} as well as the TPD are reported in subsection 3.1 and subsection 3.2, respectively.

3.1. ν_3 stretching band shape and position

Figure 2 shows the CO_2 (ν_3) asymmetric stretching fundamental for $^{12}CO_2$ when deposited at 10 K and warmed up to 90 K. The ice is deposited at 10 K, at a pressure of 2×10^{-7} mbar and warmed-up with a rate of 0.5 K/min. All the FTIR spectra have a resolution of 2 cm^{-1} and are shifted vertically for clarity. The $^{12}CO_2$ asymmetric stretching fundamental (ν_3) is located at $\sim$ 2345 cm^{-1} (4.26 µm), and is redshifted from the gas-phase value located at 2348 cm^{-1} due to interactions with the surrounding matrix environment (Isokoski (2013)). The profile is asymmetric with a prominent blue shoulder around 2350 cm^{-1}. When the CO_2 ice is warmed up, the main peak at 2345 cm^{-1} shifts to lower wavenumbers. In addition, the peak intensity increases with increasing temperature as a result of the decrease in bandwidth. Figure 3 illustrates the effect of temperature on the peak's band shape and position. In general, each spectrum can be deconvoluted into two Gaussian distributions. Gaussian 1 is the smaller one and peaks around 2351 at 10 K, and Gaussian 2 peaking at 2345 cm^{-1} for the same temperature. The figure clearly shows the redshift of both Gaussian's during warm-up as well as the decrease in FWHM for the 2345 cm^{-1} peak, going from 5.7 cm^{-1} at 10 K to 3.8 cm^{-1} at 80 K.

3.2. Thermal desorption of CO_2

A TPD curve of a pure CO_2 ice layer is shown in Figure 4. The QMS data, and in particular the molar mass of CO_2, is plotted as the ion current in Ampere as a function of temperature. This figure shows one desorption peak at 85 K. It is at this temperature

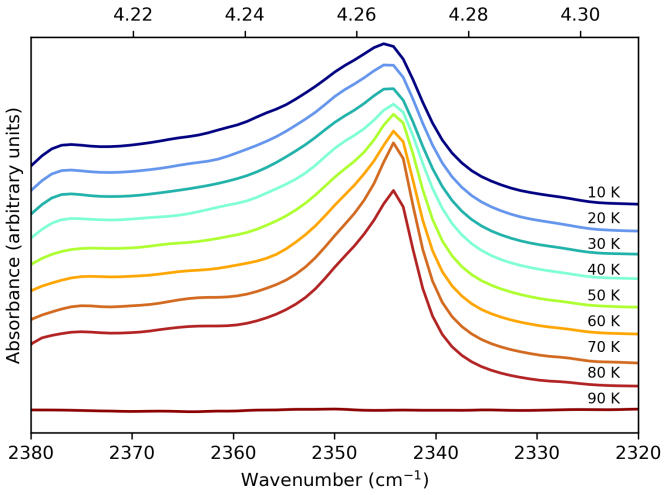

Fig. 2. Spectra over the 2380-2320 cm^{-1} range of a pure CO_2 ice deposited at 10 K and 2×10^{-7} mbar. All spectra are measured at 2 cm^{-1} resolution, and at temperatures indicated in each graph. Spectra are shifted vertically for clarity.

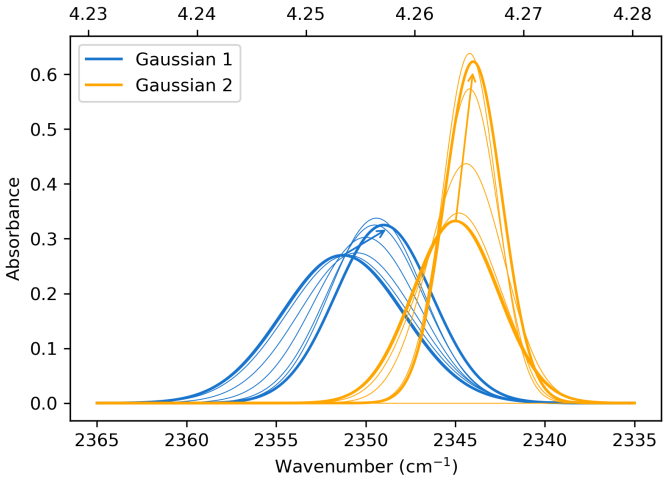

Fig. 3. Evolution of both Gaussian distributions during warm-up from 10 K to 80 K for a pure CO_2 ice. The arrows indicate the direction of evolution.

that CO_2 thermally desorbs. The desorption rate, in molecules cm^{-2} s^{-1}, of CO_2 ice is given by the Polanyi-Wigner equation:

$$\frac{dN_g(CO_2)}{dt} = \nu_i[N_s(CO_2)]^i \exp\left(-\frac{E_d(CO_2)}{T}\right) \quad (2)$$

where $N_g(CO_2)$ is the column density of CO_2 molecules desorbing from the ice surface (cm^{-2}), ν_i a frequency factor (molecules^{1-i} $cm^{-2(1-i)}s^{-1}$) for desorption order i, $N_s(CO_2)$ the column density of CO_2 molecules on the surface at time t, $E_d(CO_2)$ the binding energy in K, and T the surface temperature in K. The TPD data can be fitted using Equation 2 and the relation:

$$\frac{dN_g(CO_2)}{dt} = \frac{dT}{dt}\frac{dN}{dT} \quad (3)$$

where $\frac{dT}{dt}$ is the heating rate, 0.5 K min^{-1} in our case. Figure 5 shows the QMS data, column densities during warm-up, the Polanyi-Wigner equation and the calculated zero-order coverage. The coverage is calculated using 1-$\frac{dN_g(CO_2)}{dt}$. The TPD data is

fitted using the parameter values $\nu_0 = 0.4 \times 10^{31}$ molecules cm^{-2} s^{-1} and $E_d = 2555.78$ K for the desorption of CO_2 ice. We get to the conclusion that the coverage values determined by transmittance FTIR (green triangles) and the coverage curve computed by fitting the TPD curve recorded by QMS (solid green line) are in good agreement. There are only two remaining triangle datapoints that are poorly fitted. The issue is that a zero-order fit by definition fails when there are fewer than 4×10^{16} molecules per square centimeter of coverage, as demonstrated by Figure 5.

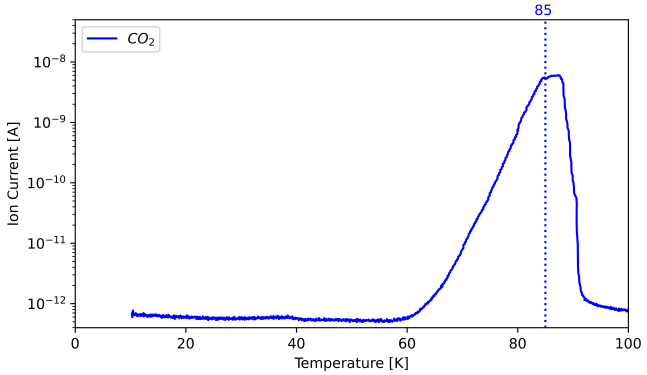

Fig. 4. TPD curve of pure CO_2 ice layer deposited at 10 K and heated at 0.5 K/min. The ion current (A) is plotted on a logarithmic scale, for a better appreciation of the curve profile, and roughly corresponds to partial pressure in mbar.

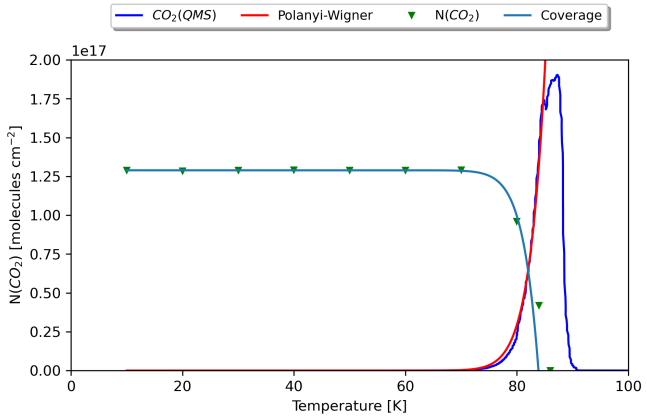

Fig. 5. Evolution of CO_2 ice, shown with triangle (from IR measurements) and TPD shown as the blue line (from QMS measurements). The TPD curve of CO_2 shown in Figure 4, is now shown on a linear scale. The solid red line is the fit corresponding to the Polanyi-Wigner. The light blue line is the calculated coverage.

4. Low CO_2 concentration and peak position

A low CO_2 content in the ice mixtures, up to 5%, is considered in this section. The important parameters of the presented experiments can be found in Table 1. Figure 6 depicts the spectra for a $1H_2O$:$0.04CO_2$ ratio deposited at 10 K. The experiment is performed with a deposition pressure of 2×10^{-7} mbar as reported in Table 1. The $^{12}CO_2$ asymmetric stretching fundamental (ν_3) can be deconvoluted into three Gaussian's, a first one peaking at 2352 cm^{-1}, a middle one at 2345 cm^{-1} and the last one at 2341 cm^{-1}. For the 10 K spectrum, the result of this deconvolution can be seen in Appendix A. The integrated absorbance area as a function of temperature is shown in the bottom panel of Figure 7. The dots represent the Gaussian peaking at 2351 cm^{-1} for 10 K, and undergoes a red shift to 2348 cm^{-1} at elevated temperatures. The triangles pointing down represent the middle Gaussian peaking at 2345 cm^{-1} for 10 K which is red shifted with 1 cm^{-1} at 80 K right before thermal desorption. The last Gaussian peaks at 2341 cm^{-1} and no changes are observed with increasing temperature.

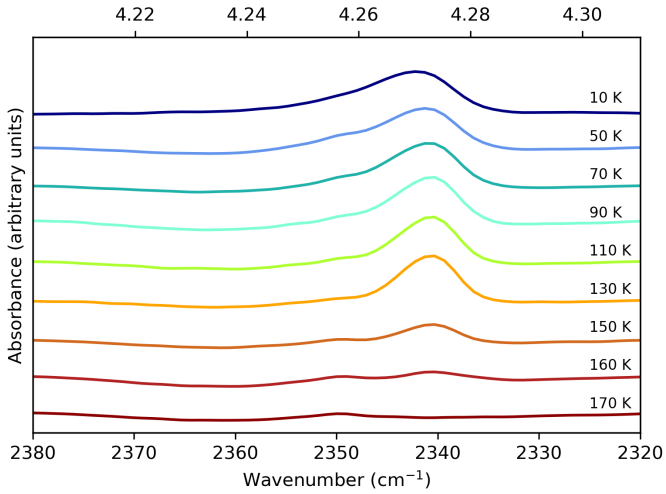

Fig. 6. Spectra over the 2380-2320 cm^{-1} range of the $1H_2O$:$0.04CO_2$ ice mixture deposited at 10 K and 2×10^{-7} mbar. All spectra at 2 cm^{-1} resolution, and at temperatures indicated in each graph. Spectra are shifted vertically for clarity.

As mentioned before, pure CO_2 thermally desorbs around 85 K. The top panel of Figure 7, showing the TPD curves of a $1H_2O$:$0.04CO_2$ ice mixture from 10 K to 180 K, presents three desorption peaks for carbon dioxide: one around 80 K, another one around 146 K, and a final one at 162 K, while only one peak appears for water, also at 162 K. The following explanation is given for the three desorption peaks of carbon dioxide:

1. Pure carbon dioxide ice thermally desorbs around 80 K, meaning that only CO_2 molecules bonded with other CO_2 molecules are desorbing.
2. Transformation from cubic to hexagonal water ice takes place at around 140 K (Martín-Doménech (2014)). During this process, carbon dioxide is pushed out of the water matrix. This peak is known as volcano desorption.
3. Co-desorption of carbon dioxide with water takes place between 160 and 170 K.

It is worth noting that carbon dioxide constantly desorbs between 80 and 146 K, as evidenced by the QMS signal being greater after the initial peak than before (see blue graph in top panel of Figure 7). This continuous desorption is caused by amorphous water ice rearrangement, which produces a change in the size and form of the porous structure (pores coalesce) when heated (Cazaux (2015)). Carbon dioxide molecules may diffuse through the pores and sublimate continuously between 80 and 146 K due to this rearrangement. The argument of diffusing carbon dioxide molecules can be verified by looking at the integrated absorbance areas of the three Gaussian peaks in the bottom panel of Figure 7. From this graph, it can be derived that pure CO_2 does indeed thermally desorb at 80 K by looking at the triangles pointing down, which represent the Gaussian peak at 2345 cm^{-1}. During this desorption of carbon dioxide molecules starting at 75 K, the peak area of the 2341 cm^{-1} location is increasing

significantly pointing towards the diffusion of the carbon dioxide molecules through the water ice structure. Once temperatures of 140 K are reached, the integrated areas of both the 2351 and 2341 cm^{-1} location are continuously decreasing during annealing confirming the amorphous water ice rearrangements. The cubic to hexagonal water-ice phase transition that occurs at 146 K is not complete, leaving a small fraction of carbon dioxide molecules to co-desorbs with water around 162 K.

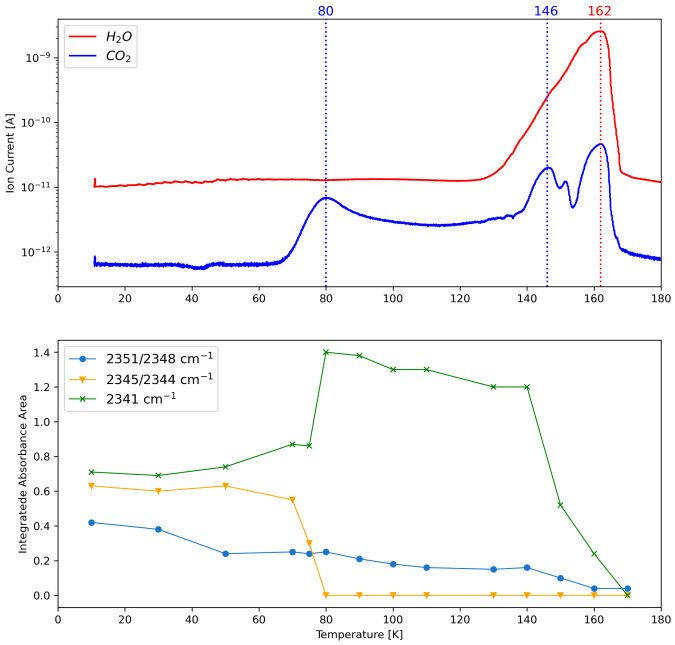

Fig. 7. Top panel: TPD curves of CO_2 and H_2O for a $1H_2O$:$0.04CO_2$ layered ice heated at 0.2 K/min. Bottom panel: integrated absorbance areas of the three Gaussian distributions as a function of temperature for a the same experiment

5. High CO_2 concentration and peak position

In this section, a high CO_2 content in the ice mixtures, above 20%, is considered. The parameters of the conducted experiments can be found in Table 1.

Figure 8 depicts the spectra between 2380-2320 cm^{-1} for a $1H_2O$:$0.25CO_2$ ice deposited at 10 K and 2×10^{-7} mbar. A broadening of the band is brought on by increasing the CO_2 concentration, which causes particle aggregation and thus creating additional trapping sites between CO_2 and H_2O (Ehrenfreund (1997)). As with the low CO_2 concentration, the spectra can be deconvoluted into three Gaussian distributions peaking at 2354 cm^{-1}, 2344 cm^{-1} and 2336 cm^{-1}, at 10 K. Due to the broadening of the CO_2 band, the shoulder on the left is shifted to the blue by 2 cm^{-1} as compared to the low CO_2 concentration spectra at 10 K. In addition, the shoulder on the right is redshifted by 4 cm^{-1}. The TPD curves and integrated absorbance area are shown in Figure 9. Again, three desorption peaks for carbon dioxide can be identified, namely at 81.8 K, 146.5 K and 161 K. The same explanation as for a low CO_2 concentration is valid for this experiment. Note the small bump in the TPD curve around 30 K is due to some amount of air inside the chamber. By checking the QMS signal of oxygen (mass 32), it was found that the signal was much higher during deposition than for all the other experiments. This means that inside the chamber there was a significant amount of air (oxygen + nitrogen). Nitrogen thermally desorbs

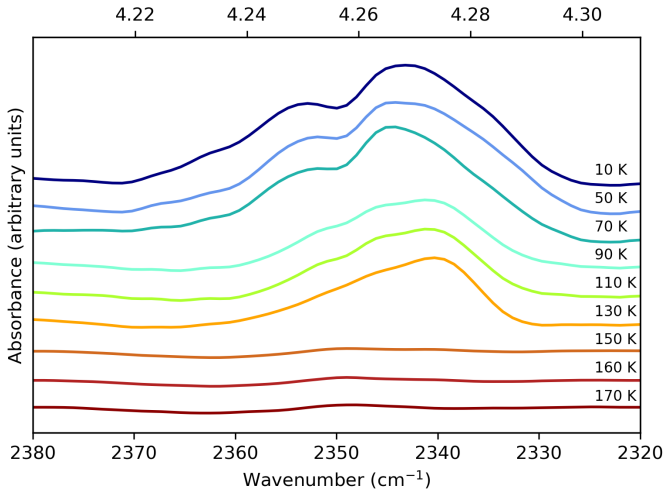

Fig. 8. Spectra over the 2380-2320 cm^{-1} range of the $1H_2O$:$0.25CO_2$ ice mixture deposited at 10 K and 2×10^{-7} mbar. All spectra are measured at 2 cm^{-1} resolution, and at temperatures indicated in each graph. Spectra are shifted vertically for clarity.

around 30 K and dragged some water and carbon dioxide with it explaining the small bump in both QMS signals. Looking at the TPD curve of carbon dioxide, the largest amount is desorbing at 81.8 K, the temperature at which pure CO_2 desorbs. The integrated absorbance area of the 2345 cm^{-1} peak drastically drops at 80 K, confirming the desorption. The bottom panel of Figure 9 clearly shows, as in the case of low CO_2 concentration, the diffusion through the water ice structure after the first desorption peak. This is shown by the increase in integrated area for the 2340 cm^{-1} peak. The transition from cubic to hexagonal water ice is not entirely complete, as a very small fraction is co-desorbing with water at 161 K.

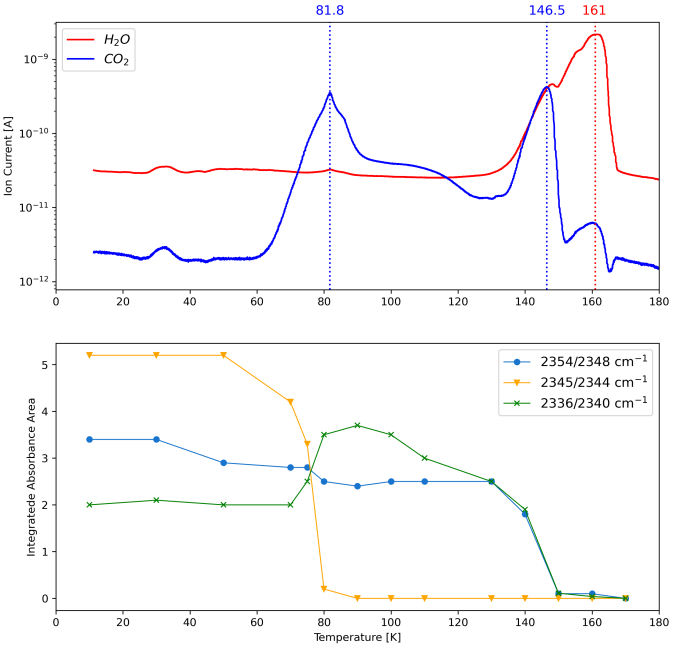

Fig. 9. Top panel: TPD curves of CO_2 and H_2O for a $1H_2O$:$0.25CO_2$ ice layer heated at 0.2 K/min. Bottom panel: integrated absorbance areas of the three Gaussian distributions as a function of temperature for a $1H_2O$:$0.25CO_2$ ice.

6. Discussion

Table 2 provides an overview of the positions of the fitted Gaussians of the asymmetric stretching bands, denoted as $\tilde{\nu_{3,1}}$, $\tilde{\nu_{3,2}}$ and $\tilde{\nu_{3,3}}$. This is done for a pure CO_2 ice, low CO_2 concentration in water ice, and high CO_2 concentration in water ice. These measurements span from 10 K, the deposition temperature, to 170 K, which corresponds to the desorption temperature of water.

For pure CO_2 ice, the positions of $\tilde{\nu_{3,1}}$ (2351.3 cm^{-1}) and $\tilde{\nu_{3,2}}$ (2345 cm^{-1}) are influenced by temperature, shifting towards the red as the temperature increases, as also demonstrated in Figure 3. In a similar manner, the positions of the two peaks $\tilde{\nu_{3,1}}$ and $\tilde{\nu_{3,2}}$ shift towards the red as the temperature increases, both when a low and high CO_2 concentration is mixed with water. Note that the $\tilde{\nu_{3,2}}$ (2344.3 cm^{-1}) shift for high concentration is much smaller than for low concentration. At 10 K, $\tilde{\nu_{3,1}}$ (2350.5 cm^{-1}) for a low CO_2 concentration closely aligns with the position in pure CO_2 ice, whereas a high concentration results in a blueshift of over 2 cm^{-1}. In addition, the $\tilde{\nu_{3,2}}$ peaks at 2344.3 cm^{-1} for a high concentration, which is redshifted by 0.7 cm^{-1} compared to the low concentration and pure CO_2 ice. The $\tilde{\nu_{3,3}}$ appears only when mixed with water. The peak position of $\tilde{\nu_{3,3}}$ in high CO_2 concentration experiences a redshift of nearly 4 cm^{-1} compared to low concentration. These shifts are due to the band broadening (Ehrenfreund (1997)), and thus shifting the Gaussian fits, resulting from increased CO_2 concentration in the water ice (see Appendix B.1.).

The thermal evolution of the CO_2 $\tilde{\nu_{3,1}}$, $\tilde{\nu_{3,2}}$ and $\tilde{\nu_{3,3}}$ are reported in Figure 10. This figure depicts the three Gaussians from 10 K to 170 K. The top panel shows a low CO_2 concentration whereas the bottom panel corresponds to a high concentration. The Gaussians for 10 K are highlighted for clarity representing the beginning of the experiment. The thicker arrows indicate the direction of evolution with increasing T, clearly illustrating how $\tilde{\nu_{3,3}}$ shifts to the blue only for a high concentration. For a low concentration, the peak intensity of $\tilde{\nu_{3,3}}$ first increases after 80 K which becomes CO_2 embedded in the water ice matrix, as illustrated in the top panel of Figure 10. At 80 K, which is the desorption temperature for pure CO_2, $\tilde{\nu_{3,1}}$ shifts to lower wavenumbers for both low and high concentrations. At 140 K, the integrated absorbance areas decrease due to the transition from cubic to hexagonal ice structure (Martín-Doménech (2014)). It is worth noting that in Table 2, for temperatures above 160 K, $\tilde{\nu_{3,1}}$ shifts back towards the blue, ultimately resulting in a single peak at around 2348 cm^{-1} at 170 K for low concentration and 2349.1 cm^{-1} for high concentration.

Furthermore, the influence of deposition pressure on the peak positions has been explored. To investigate this, an experiment was conducted with a deposition pressure of $8{\times}10^{-7}$ mbar and a 4% CO_2 concentration. Upon analyzing the peak positions at 10 K, it was observed that the positions of $\tilde{\nu_{3,2}}$ and $\tilde{\nu_{3,3}}$ were consistent with the experiment conducted at a lower deposition pressure. However, $\tilde{\nu_{3,1}}$ peaked at approximately 2351.5 cm^{-1}. The higher deposition pressure induced changes in the ice morphology, rendering it more porous. A DFT simulation, reported in Appendix A.4., which shows the effect a pore has on an amorphous CO_2 ice. Due to the higher deposition pressure, the ice produced is more porous, and therefore undergoes greater reorganization during the warm-up process. At 10 K, $\tilde{\nu_{3,1}}$ peaks around 2351.5 cm^{-1} which is a 1 cm^{-1} blue shift

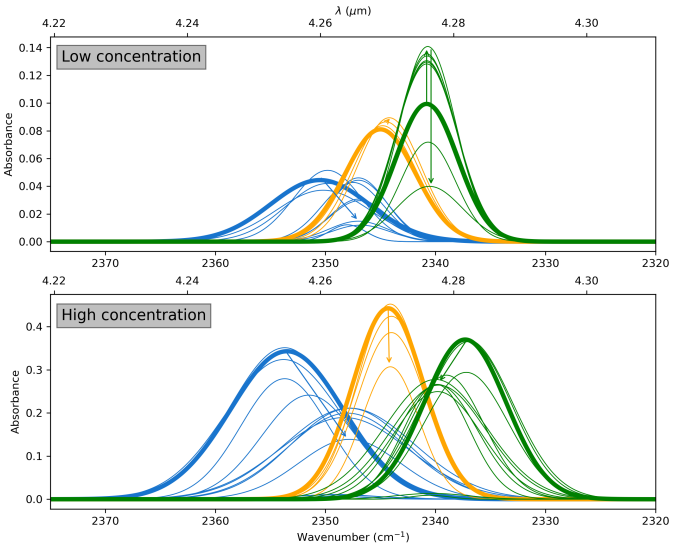

Fig. 10. Three Gaussian distributions plotted from 10 K to 170 K, for a low and high CO_2 concentration in the ice. Blue represents $\tilde{\nu_{3,1}}$, orange $\tilde{\nu_{3,2}}$ and green $\tilde{\nu_{3,3}}$. The bold graphs indicate the beginning of the experiment at 10 K. The arrows indicate the direction of evolution.

compared to the low deposition pressure. By the time the temperature reached 50 K and the CO_2 became crystalline, the reorganization was complete. At this point, $\tilde{\nu_{3,1}}$, $\tilde{\nu_{3,2}}$, and $\tilde{\nu_{3,3}}$ were all peaking at approximately 2349.8 cm^{-1}, 2344.5 cm^{-1}, and 2340.6 cm^{-1}, respectively. These are similar peak locations as for the low deposition pressure.

The assignment of the different Gaussian peaks is discussed in this section. As previously mentioned, when CO_2 is mixed with water, three distinct peaks emerge. The first of these, $\tilde{\nu_{3,1}}$, peaks at approximately 2351 cm^{-1} for low CO_2 concentration and around 2353 cm^{-1} for high concentration. This band can be attributed to pure CO_2 ice meaning that this peak does not need other type of ice to be present, but reflects the porosity of CO_2. However, for CO_2 mixed with water, this peak is still present above the 80 K temperature, which implies that the carbon dioxide molecules must be interacting with the water, or are trapped in the ASW. Other explanations for this band location is that carbon dioxide is in a "complexed" form with water, as suggested by Chaban (2007). A blue shift of 5 cm^{-1} compared to the pure CO_2 ice is observed when bonded with one water molecules, and 10 cm^{-1} with two. Furthermore, the symmetric O-H stretching band undergoes a redshift when complexed with two water molecules and the intensity increases significantly. In this work, for a 4% CO_2 concentration, there was no increase in intensity nor a redshift at 10 K for the symmetric O-H stretching band when compared to that of a pure H_2O ice, ruling out the possibility of a complexed CO_2. Another explanation for the attribution of this peak location is related to the dangling bonds. As suggested by Matsuda (2018) for CO, two bands are assigned, namely CO molecules interacting with the OH dangling groups (CO-dangling OH) and CO molecules interacting with the oxygen atoms of the surface water molecules (CO-bonded OH). It was found that the area of the CO-dangling band increases when the temperature was increased meaning that CO molecules partially sublimate and diffuse to CO-dangling OH groups on the surface of the ASW pores. To conclude, this work shows with the experimental data and a DFT simulation that this peak can be attributed to the porosity of the ice.

The peak at approximately 2345 cm^{-1}, labeled as $\nu_{3,2}$, can be attributed to pure CO_2. This is corroborated by the desorption temperature of pure CO_2, which falls in the range of 80-85 K (as illustrated in Figure 4). For both low and high CO_2 concentrations, this peak disappears at temperatures exceeding 80 K, as evidenced in Table 2. This is also referred to as the CO_2-*ext* where the interaction with water is quite weak as it would be if CO_2 were superficially adsorbed, as proposed by Gálvez (2007).

The third peak, $\nu_{3,3}$, arises when CO_2 is mixed with water and peaks around 2340.7 cm^{-1} in low CO_2 concentrated water ice. This peak is likely the outcome of CO_2 interacting with water molecules. This peak is also referred to as CO_2-*int* in previous work, where CO_2 molecules enter the pores of ASW. Due to the interaction of CO_2 with surrounding water, a slight weakening of the C-O bond will result. The integrated absorbance area of $\nu_{3,3}$ diminishes as the water ice transitions to a hexagonal structure and co-desorbs with water.

7. Application to icy moons

In this section, we used JWST ERS data from Ganymede (Bockelée-Morvan (2023)) and Europa (Villanueva (2023)) to study the position and evolution of the CO_2 bands as latitude and longitude. Our goal is to assign the different CO_2 bands already reported in the literature (Bockelée-Morvan (2023);Villanueva (2023)) to physical state of CO_2 ice.

7.1. Ganymede: Latitude Spectra

This section will only discuss the latitude and longitudinal spectra of Ganymede's leading hemisphere as the same trends are observed on the trailing hemisphere.

Figure 11 shows the CO_2 band observed on Ganymede as a function of the latitude, as reported in Bockelée-Morvan (2023). The latitudinal variations of the CO_2 band and its asymmetric band shape support the view that different CO_2 physical states are involved. The 4.27-μm (2342 cm^{-1}) peak is stronger across the northern latitudes, which are colder and more enriched in water ice (Bockelée-Morvan (2023);Trumbo (2023)). Across the equatorial latitudes, the 4.25 μm (2353 cm^{-1}) peak dominates. Ganymede has an average surface temperature around 100 K, with a maximum of 160 K at the equator (de Kleer (2021)). The Gaussian fits are represented with dotted lines, and plotted for each range of latitudes. Each latitude spectrum can be deconvoluted into two Gaussian distribution. When analyzing the results, one of the Gaussians peaks at 2341.7 cm^{-1} at the poles and moves slightly inward with increased temperature. This is in agreement with the $\nu_{3,3}$ band observed experimentally, which is shifting slightly to the blue as the temperature increases. Moving closer to the equator, this peak shifts even more to the blue, peaking at 2342.5 cm^{-1}. The second Gaussian peaks around 2350.3 cm^{-1} at the North pole and around 2350.9 cm^{-1} at other latitudes. This is also in agreement with the $\nu_{3,1}$ band observed experimentally, which is blueshifting from temperature above 150 K. This coincides with the surface temperature at Ganymede's equator.

7.1.1. Longitudinal variations of CO_2

The longitudinal spectra for Ganymede's leading hemisphere are shown in Figure 12. The solid lines are JWST spectra and the colors indicate different longitudinal ranges. The variations of

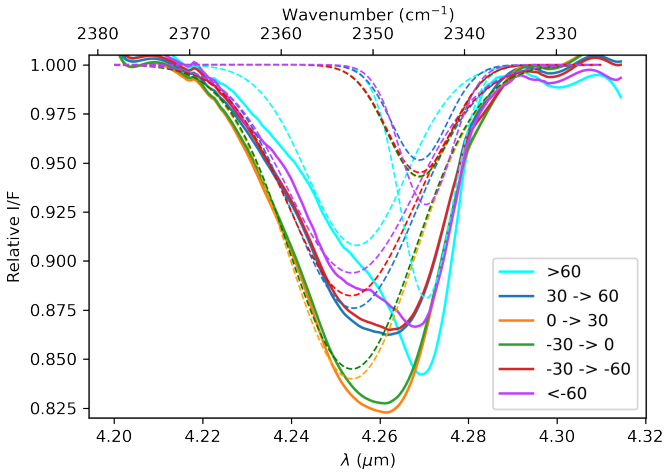

Fig. 11. Latitude spectra of Ganymede's leading hemisphere acquired with JWST. Colors are used to indicate different latitude ranges. The dotted lines represent the Gaussian fit of each individual spectrum which is deconvoluted in two Gaussians.

the CO_2 band position and intensity are shown in the figure for latitudes between 60 degrees North and 60 degrees South. The morning limb is represented by the 120-150 W spectrum (blue), whereas the evening limb is represented by the 30-60 W spectrum (red). Each spectrum is deconvoluted into two Gaussian distributions, which are shown by dotted lines. As previously stated, more porous ice can lead to a blueshift of the peak centered about 2351 cm^{-1}. When comparing morning (blue) to evening (red), there is a blueshift as well as an increase in peak intensity. During the day, UV irradiation strikes Ganymede's surface, making water ice become more amorphous (Bockelée-Morvan (2023)). This demonstrates that the peak centered about 2351 cm^{-1} is affected by ice porosity due to CO_2 molecules dangling bond present in the pores, or eventually in cracks created in the ice when the temperature fluctuates from day to night.

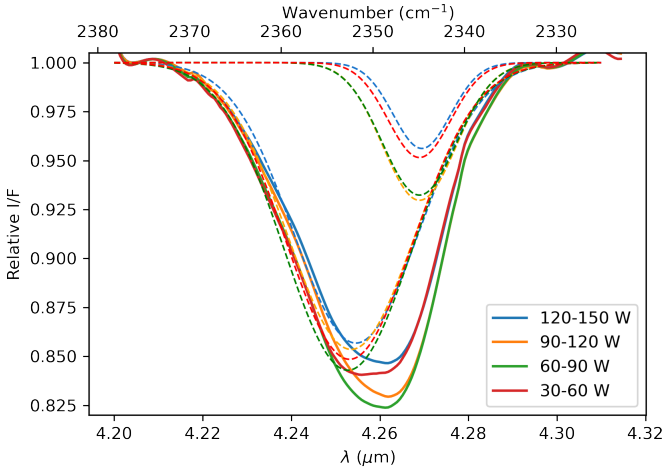

Fig. 12. Longitudinal spectra of Ganymede's leading hemisphere acquired with JWST. The longitudes are taken between 60 degrees North and 60 degrees South in latitude. The spectrum for 120-150 W represents the morning limb of the leading edge and the evening limb by the 30-60 W spectrum. Colors are used to indicate different longitudinal ranges. The dotted lines represent the Gaussian fit of each individual spectrum which is deconvoluted in two Gaussians.

Table 2. Band positions ($\tilde{\nu}$) for all three fitted Gaussians as a function of temperature. This is done for a pure CO_2 ice, a low CO_2 concentration and a high CO_2 concentration.

	Pure CO_2			Low CO_2			High CO_2		
T (K)	$\nu_{3,1}$ (cm^{-1})	$\nu_{3,2}$ (cm^{-1})	$\nu_{3,3}$ (cm^{-1})	$\nu_{3,1}$ (cm^{-1})	$\nu_{3,2}$ (cm^{-1})	$\nu_{3,3}$ (cm^{-1})	$\nu_{3,1}$ (cm^{-1})	$\nu_{3,2}$ (cm^{-1})	$\nu_{3,3}$ (cm^{-1})
10	2351.3	2345	-	2350.5	2345	2340.8	2353.5	2344.3	2337.3
30	2351	2344.8	-	2350.2	2344.8	2340.8	2353.7	2344	2337
50	2350	2344.3	-	2349.8	2344.5	2340.7	2353.8	2344	2337.1
70	2349.4	2344.2	-	2349.8	2344.2	2340.6	2353.7	2344.1	2337.2
80	2349	2344	-	2347.5	-	2340.7	2351.5	2344.1	2339
90	-	-	-	2347	-	2340.7	2348	-	2339.7
100	-	-	-	2347	-	2340.8	2348.3	-	2340
110	-	-	-	2347	-	2340.7	2347.8	-	2339.9
130	-	-	-	2346.9	-	2340.8	2347.8	-	2339.8
140	-	-	-	2347	-	2340.8	2347.8	-	2339.9
150	-	-	-	2346.8	-	2340.7	2349	-	2340.3
160	-	-	-	2348	-	2340.6	2349.3	-	2340.5
170	-	-	-	2348	-	-	2349.1	-	-

7.2. Europa

Figure 13 shows the CO_2 band observed on Europa as a function of the latitude, as reported in Villanueva (2023). The 4.27-μm (2342 cm^{-1}) peak is stronger across the northern latitudes, which are colder and more enriched in water ice (Trumbo (2023)). Across the equatorial latitudes, the 4.25 μm (2353 cm^{-1}) peak dominates. The temperature on Europa ranges from 60 K at the poles to around 110 K at the equator, making it colder than on Ganymede. The Gaussian fits are represented with dotted lines, and plotted for each range of latitudes. Each latitude spectrum can be deconvoluted into two Gaussian distribution, as seen in Figure 13. The 4.27 μm (2342 cm^{-1}) feature shifts inwards when moving closer to the equator, from 2340.9 cm^{-1} for 30 to 60 degrees North to 2341.2 cm^{-1} at the equator. This is in agreement with the $\nu_{3,3}$ band position observed experimentally, which peaks around 2340.8 cm^{-1}. The second Gaussian $\nu_{3,1}$, peaking at 2353.5 cm^{-1}, is shifted to the blue by around 3 cm^{-1} when compared to Ganymede due to the colder ice temperature resulting in a more porous ice.

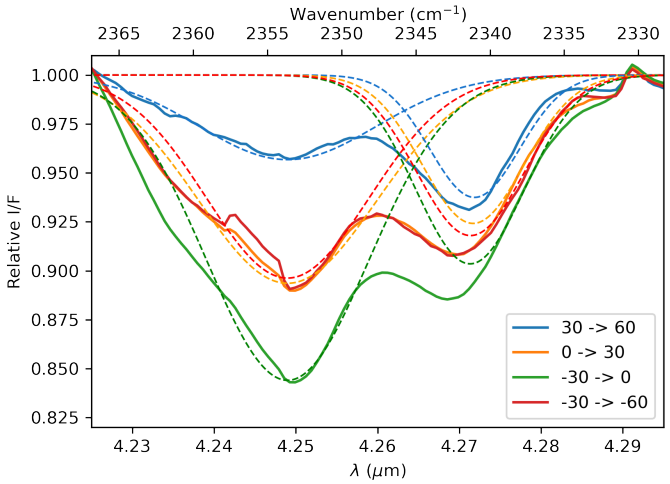

Fig. 13. Latitude spectra of Europa's leading hemisphere acquired with JWST. Colors are used to indicate different latitude ranges. The dotted lines represent the Gaussian fit of each individual spectrum, each consisting of two Gaussians.

The main conclusion of this section is that CO_2 trapped in water ice can account for the whole CO_2 band observed in Ganymede's leading hemisphere and Europa's spectra. In the boreal region of Ganymede's leading hemisphere, the CO_2 band is dominated by a high wavelength component at $\sim$ 4.27 μm (2342 cm^{-1}), consistent with CO_2 trapped in amorphous water ice. The Gaussian at 4.25 μm (2353 cm^{-1}) is shown to be depending on the pores present in the ice, in which CO_2 molecules, when present in pores can exhibit CO_2 dangling bonds. The band assignment of $\nu_{3,1}$ to CO_2 in pores has been suggested (or other words) by our experiments combined with DFT simulations. It should be noted that the 4.25 μm (2353 cm^{-1}) band depends on the concentration of CO_2 in the water ice, which will make the band shift.

8. Conclusions

The examination of CO_2 ice behavior on icy moons has offered intriguing revelations about its interaction within these distinct environments. Moreover, aligning laboratory findings with JWST data from Ganymede and Europa bridges the gap between theory and real-world celestial surfaces, enriching our understanding of these moons' environments. These conclusions significantly contribute to our comprehension of CO_2's role in icy settings, unveiling crucial insights into the complexities of these celestial bodies. In this study we combined FTIR measurements and TPD experiments to assign the different CO_2 bands observed.

1. The stretching band observed at 2345 cm^{-1} for pure CO_2 ice at 10 K consists of two distinct Gaussians: $\nu_{3,1}$ peaks at 2351.3 cm^{-1}, and $\nu_{3,2}$ peaks at 2345 cm^{-1}. The band's shape evolves during warm-up from 10 K to 80 K, exhibiting a redshift in both Gaussians. The TPD data indicates a desorption peak at 85 K, suggesting thermal desorption of CO_2 from the ice layer. The thermal desorption process is effectively modeled and fitted using the Polanyi-Wigner equation, allowing the calculation of coverage values that align well with the coverage determined through transmittance FTIR measurements.
2. CO_2 mixed with water ice (low and high concentration) exhibits multiple peaks, of which two are the same as for pure CO_2. The presence of three peaks, $\nu_{3,1}$ at 2351 cm^{-1}, $\nu_{3,2}$ at

2345 cm^{-1}, and $\nu_{3,3}^{\sim}$ at 2341 cm^{-1} at 10 K demonstrate the complexity of CO_2 interaction within water ice. The different CO_2 bands are assigned as follows: $\nu_{3,1}^{\sim}$ is assigned to CO_2 dangling bonds in which CO_2 molecules are found in pores or cracks, $\nu_{3,2}^{\sim}$ is due to several CO_2 molecules trapped in the ice (segregated) and $\nu_{3,3}^{\sim}$ is CO_2 interacting with water ice, which means embedded in the water ice.

3. The thermal desorption analyses allowed to assign distinct peaks in the desorption curves, suggesting different desorption behaviors for CO_2 within the ice. Both concentrations display similar desorption patterns. Initial CO_2 desorption occurs around 80 K, followed by peaks at 146 K and 162 K, indicating various CO_2-water interactions during ice phase transitions. Continuous desorption between 80 and 146 K is observed, driven by the amorphous water ice rearrangement, facilitating CO_2 diffusion through the ice matrix pores.
4. The JWST NIRSPEC spectra of Ganymede's leading hemisphere reveals significant variations in the CO_2 band across different latitudes. Two main CO_2 bands have been observed, that we assigned to $\nu_{3,1}^{\sim}$ (4.25 μm/2353 cm^{-1}) and $\nu_{3,3}^{\sim}$ (4.27 μm/2342 cm^{-1}). The dominance of $\nu_{3,1}^{\sim}$ (4.27-μm/2342 cm^{-1}) in northern latitudes, associated with colder regions enriched in water ice, contrasts with the prevalence of $\nu_{3,3}^{\sim}$ (4.25-μm/2353 cm^{-1}) in equatorial latitudes. Gaussian fits of the spectra suggest two distinct physical states of CO_2 that shift with temperature, which confirm the assignments from our laboratory findings. The CO_2 peaks observed on Ganymede with latitude could be attributed to an increase in temperature, showing that in the poles CO_2 is well embedded with water ice.
5. The longitudinal spectra for Ganymede's leading hemisphere indicates variations in CO_2 spectra from morning to evening. The analysis, focused on latitudes between 60 degrees North and 60 degrees South, shows that the observed blueshift of the $\nu_{3,1}^{\sim}$ peak centered around 2351 cm^{-1} could be linked to the porosity of the ice. Morning and evening limb spectra exhibit shifts in peak position and intensity, attributed to the influence of UV irradiation during the day as well as the variation of the temperature which could create pores coalescence or cracks.

References

C. González Díaz, H. Carrascosa, G. M. Muñoz Caro, M. Á. Satorre, & Y.-J. Chen, MNRAS 000, 1-21, 2022
G. M. Muñoz Caro, A. Jiménez-Escobar, J. Á. Martín-Gago, C. Rogero, C. Atienza, S. Puertas, J. M. Sobrado, & J. Torres-Redondo, 2010, A&A, 522, A108
P. Ehrenfreud, A.C.A. Boogert, P.A. Gerakines, A.G.G.M. Tielens, & E.F. van Dishoeck, 1997, A&A, 328, 649-669
J. Crovisier, 2006a, Mol. Phy., 104 (16-17), 2737-2751
J. Crovisier, 2006b, Faraday Discuss., 133, 375-385
G. M. Chaban, M. Bernstein, & D. P. Cruikshank, 2007, Icarus, 187, 592-599
O. Gálvez, I.K. Ortega, B. Maté, M.A. Moreno, B. Martín-Llorente, V.J. Herrero, R. Escribano, & P.J. Gutiérrez, 2007, A&A, 472, 691-698
K. Isokoski, C.A. Poteet, & H. Linnartz, 2013, A&A, 555, A85
S. Cazaux, J.-B. Bossa, H. Linnartz, & A.G.G.M. Tielens, 2015, A&A, 573, A16
R. Martín-Doménech, G.M. Muñoz Caro, J. Bueno, & F. Goesmann, 2014, A&A, 564, A8
S. Matsuda, M. Yamazaki, A. Harata, & A. Yabushita, 2018, Chem. Lett., 47, 468–471
W.M. Grundy, L.A. Young, & E.F Young, 2003, Icarus, 162, 222-229
B.J Buratti, & 28 colleagues, 2005, Astrophys. J., 622 (2), L149-L152
E. Dartois, K. Pontoppidan, W.-F. Thi, & G.M. Muñoz Caro, 2005,A&A ,444,L57–L60
B.T. Draine, 2003,A&A ,41, 241-289
S.A. Sandford, & L.J. Allamandola, 1990, Astrophys. J. ,355, 357-372
P. Ehrenfreund, O. Kerkhof, W.W. Schutte, A.C.A. Boogert, P.A. Gerakines, E. Dartois, L. d'Hendecourt, A.G.G.M. Tielens, E.F. van Dishoeck, & D.C.B. Whittet, 1999,A&A ,350, 240-253
M.P. Bernstein, D.P. Cruikshank, & S.A. Sanford, 2005, Icarus , 179, 527-534
G. Kumi, S. Malyk, S. Hawkins, H. Reisler, & C. Wittig, 2006, J. Phys. Chem. , A 110, 2097-2105
S. Malyk, G. Kumi, H. Reisler, & C. Witting, 2006, J. Phys. Chem., A 111, 13365-13370
W. Hagen, A. Tielens, & J. M. Greenberg, 1981, J. Phys. Chem. ,56, 367
M. Bouilloud, N. Fray, Y. Benilan, H. Cottin, M.-C. Gazeau, & A. Jolly, 2015, MNRAS ,451, 2145-2160
D. Bockelée-Morvan, et al., 2023, A&A.
G. L. Villanueva, et al., 2023, Science, 381, 6664, 1305-1308.
S.K. Trumbo, et al., 2023, Science Advances, 9, 29
S.K. Trumbo and M. E. Brown, 2023, Science, 381, 6664, 1308-1311
K. de Kleer et al., 2021, Planet. Sci. J. 2, 5

4

Conclusions and Future Work

In this chapter, the conclusions will be presented in Section 4.1, addressing the initial research questions. Additionally, Section 4.2 will provide recommendations for future work.

4.1. Conclusions

This section uses the work reported in the scientific article and the supplementary appendices to answer the established research questions.

1. **What specific spectral features in the infrared range are indicative of certain types of ices and surface features on icy moons?**

   In the infrared range, the spectral features of carbon dioxide ices and surface features on icy moons can be identified based on characteristic absorption bands. For this research, the focus is on the asymmetric stretching mode of CO_2 which typically peaks in the range of 2330 and 2345 cm^{-1}. However, it is theorized that CO_2 trapped in amorphous water ice results in a red shift at the poles of Ganymede. A blue shift and band broadening, which is present at the equatorial latitudes, could indicate the likely presence of CO_2 adsorbed or trapped on non-icy materials, such as minerals or salts.

2. **How can these characteristics be attained through laboratory experiments?**

   The Interstellar Astrochemistry Chamber (ISAC) is employed to experimentally investigate CO_2 ice under simulated interstellar medium conditions. The ultra-high vacuum chamber, with a base pressure of 4×10^{-11} mbar, features a closed-cycle helium cryostat for precise temperature control down to 8 K. Gas mixtures of H_2O and CO_2 of varying ratios are introduced, and Fourier-transform infrared spectroscopy (FTIR) captures spectral changes during ice deposition. The experiments include temperature programmed desorption (TPD) and laser interferometry to monitor ice thickness, providing insights into the behavior of the CO_2 stretching mode under different conditions.

3. **What is the desorption pattern of CO_2:H_2O mixtures? And what effect does the heating ramp have on the desorption peaks?**

   Thermal desorption analysis reveal discrete peaks in the desorption curves, implying various CO_2 desorption behaviors inside the ice. Desorption patterns are comparable for low and high CO_2 concentrations in water ice. The first desorption of CO_2 occurs about 80 K, followed by peaks at 146 K and 162 K, showing diverse CO_2-water interactions during ice phase transitions. The amorphous water ice rearrangement causes continuous desorption between 80 and 146 K,

allowing CO_2 passage via the ice matrix pores. It was found that a higher warm-up rate delays the desorption of the carbon dioxide and water molecules by just a few Kelvin.

4. **What effect does the abundance of CO_2 in water ice have on the asymmetric stretching band?**

   The abundance of CO_2 in water ice significantly affects the asymmetric stretching band in CO_2/H_2O mixtures. When the water ice content surpasses a few percent, additional trapping sites are formed, leading to a peculiar profile of the CO_2 stretching mode. This results in the appearance of a second band at 2330 cm^{-1}, causing a broadening and asymmetry in the band shifted by about 12 cm^{-1} to lower frequency. The characteristics of this second band change with varying concentrations of H_2O and CO_2. In mixtures where H_2O is more abundant, the band position peaks closer to pure CO_2, and the width of the peak is reduced.

5. **How do laboratory spectra relate to JWST observations?**

   Laboratory spectra are usually in transmittance and serve as a reference for interpreting the features observed by JWST. From these experiments, it was found that the ν_3 band can be deconvoluted into two or three Gaussian distributions, depending on temperature. These band positions are analyzed as a function of temperature and concentration to establish patterns and to assign these Gaussian bands to different molecular interactions in the ice. Afterwards, the same deconvolution process is done with JWST observations of Ganymede's leading hemisphere. The band locations were compared to the one in the lab in order to characterize the carbon dioxide on Ganymede.

4.2. Recommendations for Future Work

Future work suggestions will be grouped into two categories: experimental and observations. Analyzing spectral data from JWST is still in its early stages, which means there is still a lot of work to be done. These suggestions have been whittled down to serve as a reasonable next step in this research.

4.2.1. Experimental

- In this research several experiments are carried out with a varying CO_2:H_2O ratio. However, the effect of weathering (radiation) on these ice are not tested in the lab. It was concluded in the paper that UV irradiation has an effect of the CO_2 band position when comparing the morning to evening spectrum on Ganymede's leading hemisphere. Exposing the ice in the lab to a substantial amount of radiation and time can give more insights in the effect of weathering on the ice structure and band position.
- Experiments with a very low CO_2 concentration in the water ice can be deposited at 10 K, warmed up until 150 K and again cooled down afterwards. This resembles the morning to evening cycle on Ganymede, where the ice is warmed up and cooled down every day. This can give more insight in the CO_2 band position and can be linked to the observations.
- In order to see the variation in peak position of the 2351 cm^{-1} peak, experiments can be carried out with varying porosity. This can be achieved by changing the deposition pressure, although this is also strongly related to how the ice is deposited. As in this research, this can be done for a pure CO_2 ice and for mixtures with water.
- Additional DFT simulations can be done, where the accuracy of the system better resembles the wavenumbers from the lab and on the icy moons.

4.2.2. Observations

- In this research, the latitudes and longitudes at a specific time are analyzed. Looking at the same locations, but at different times can shed light on the weathering (UV) effects on the CO_2 peak position and intensity. By doing so, it can be analyzed if the ice becomes more porous over time. This can then be compared to the additional lab spectra, as mentioned above.

- In this research the leading hemisphere is analysed, an addition would be to also plot the latitudes and longitudes of the trailing hemisphere. This can give more information on the conditions of both hemispheres by comparing leading to trailing.
- Latitude and longitudinal spectra of Europa can give insight into the different process present on this icy moon. A comparison can be made between Ganymede and Europa and similarities and discrepancies can be identified. After all, they are both orbiting Jupiter, and Europa is in general a bit colder.

A

Journal Clarifications

A.1. Estimation Gas Mixture Ratio

In order to determine the gas mixture ratio of the ice, the column density of both molecules must be calculated. The procedure for doing this is explained here and will be done for a experiment with 4 % CO_2 in the ice. The same procedure is applied for other experiments.

The integration of the infrared absorption band yields the column density N of the ice layer accreted on the cold substrate in molecules cm^{-2} with the following formula:

$$N = \int_{band} \frac{\tau_\nu d\nu}{A} \tag{A.1}$$

with A the band strength in cm molecules^{-1}, τ_ν the optical depth of the band and dν the wavenumber differential in cm^{-1}. The integrated absorbance is equal to 0.43 $\times$ τ, where τ is the integrated optical depth of the band. The ratio is calculated by dividing the column density of CO_2 by the one for H_2O and results in:

$$ratio = \frac{N_{CO_2}}{N_{H_2O}} \tag{A.2}$$

For both molecules, the band strength of the pure ices are used, resulting in the H_2O band set to 2.0$\times$10^{-16} cm molecules^{-1}. The band strength for the pure CO_2 anti-symmetric stretching band equals 7.6$\times$10^{-17} cm molecules^{-1}. Another method used by Gerakines et al. 1995 suggests to calculate new band strengths ratios for both molecules. However, it was found that these ratios were in the range of 0.95 and 0.99 for both molecules for low CO_2 concentrations. This method failed to provide reliable results when the concentration was beyond 20 % of CO_2. The first step of the procedure is to subtract the reference spectrum (orange) from the IR ice spectrum (blue), which is visualized in Figure A.1. This is done to account for variations in the IR source from day to day and compensation of atmospheric H_2O and CO_2 interfering with the IR beam before it reaches the IR detector. It must be mentioned that for each experiment a new reference spectrum is taken. To compute the integrated intensities of the H_2O stretching peaks, the measured peak positions and the integration bounds in cm^{-1} (μm) are taken between a lower bound of 3000 (3.33) to an upper bound of 3600 (2.78). For the CO_2 anti-symmetric stretching mode this is with a lower bound of 2330 (4.29) and upper bound 2360 (4.24). This is displayed in Figure A.2 for CO_2 and Figure A.3 for H_2O. The area, colored in gray, is calculated using the trapezoidal rule. The results at 10 K for this experiment are an area of 124.3 for the H_2O band and 1.78 for the CO_2 band. Using Equation A.2 and filling in the numbers results in:

$$ratio = \frac{\frac{1.78}{7.6 \cdot 10^{-17}}}{\frac{124.3}{2 \cdot 10^{-16}}} = 3.77\,\%\ CO_2 \tag{A.3}$$

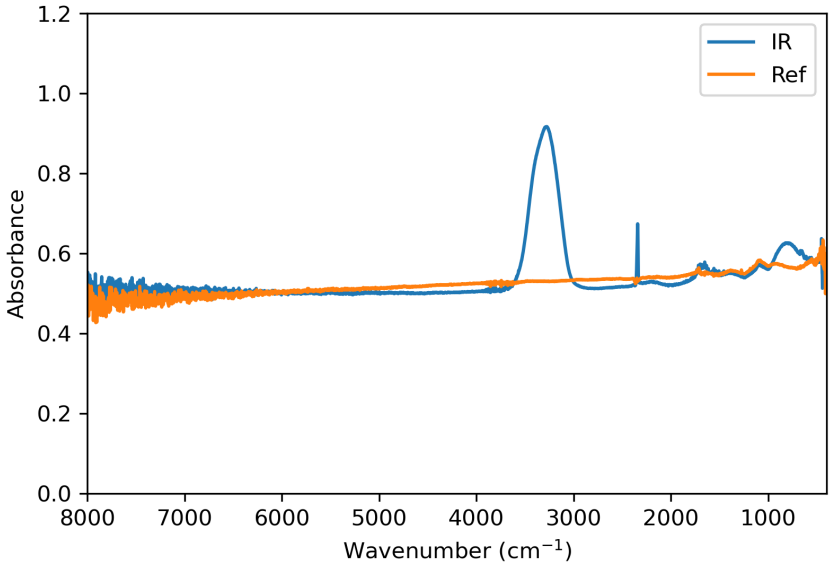

Figure A.1: Reference spectrum plotted in orange together with the IR spectrum of the ice at 10 K and 4% of CO_2 in blue.

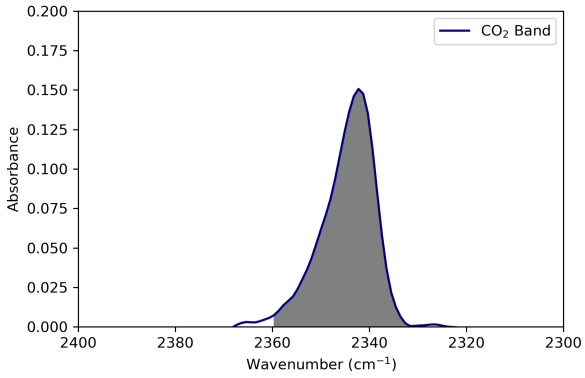

Figure A.2: Spectrum at 10 K and 4% CO_2 plotted from 2400 to 2300 cm^{-1}. The area under the absorbance peak is gray and is calculated using the trapezoidal rule from an upper bound of 2360 to a lower bound of 2330 cm^{-1}.

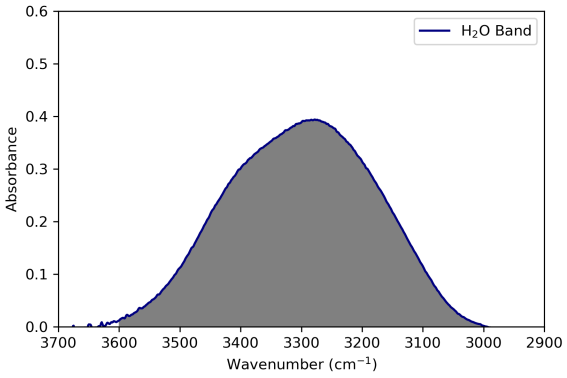

Figure A.3: Spectrum at 10 K and 4% CO_2 plotted from 3700 to 2900 cm^{-1}. The area under the absorbance peak is gray and is calculated using the trapezoidal rule from an upper bound of 3600 to a lower bound of 3000 cm^{-1}.

A.2. Ice Thickness Measurements

Signal laser interference is applied to measure the thickness of the ice. One wave is reflected from the ice surface and one transmitted through the ice and then reflected from the surface of the cold substrate used for ice deposition. The reflection of both waves, shown in Figure A.4, creates an interference pattern as the result of ice thickness increase during deposition. If the deposition rate is constant, this interference forms a periodic pattern that allows estimation of the ice thickness. In practice, we estimated the ice thickness deposited during the time lapse between two consecutive minima as:

$$d = \frac{\lambda_0}{2n_{ice}\cos\theta_t} \tag{A.4}$$

where n_{ice} depends on the ice deposition temperature, λ_0 = 632.8 nm for the He-Ne laser, and the angle θ_t is

$$\theta_t = \arcsin\left(\frac{n_{vac}\sin\theta_i}{n_{ice}}\right) \tag{A.5}$$

with $\theta_i = 3°$. For the derivations of the above mentioned variables, see González Díaz et al. 2022.

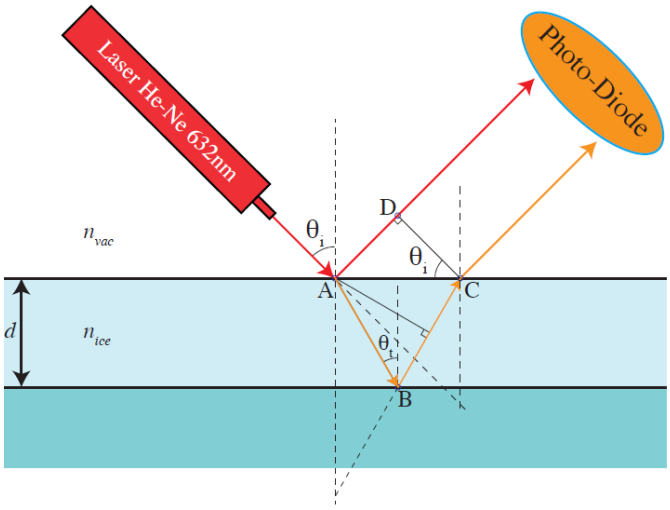

Figure A.4: Sketch of the thin film interference principle, with the two reflections shown (González Díaz et al. 2022).

A schematic diagram of the working of the python code used to determine the ice thickness is given by Figure A.5. The input, namely the signal laser interference file, results from the laser measurements made during the experiments. The .dat file contains several variables, e.g.: time, temperature, pressure, photon dose, laser intensity,... For the purpose of this research, the laser intensity, in Watt, is plotted against time which is measured in seconds. As a result of the signal laser interference principle, a clear sinusoidal wave will be visible as shown in the upper graph on Figure A.6. From this signal, it is very clear to define the time range during deposition. It is for this time range that several minima are to be calculated. These minima are made visible by the cross marks on the upper graph of Figure A.6. The thickness of the ice can be defined as:

$$d = t_{minima} \cdot dr_{avg} \tag{A.6}$$

where t_{minima} is the time between two consecutive minima and dr_{avg} represent the average deposition rate. Since the equation makes use of the average deposition rate, the thickness of the ice will increase linearly as shown in the bottom graph on Figure A.6.

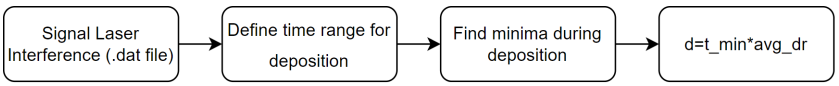

Figure A.5: Diagram to illustrate the working principle of the Python code for measuring the ice thickness.

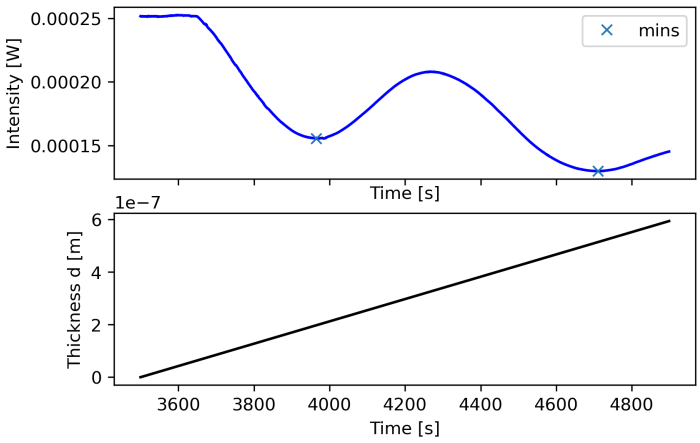

Figure A.6: Ice deposition at 10 K for a $1H_2O$:0.04 CO_2 mixture. Top panel: two laser interference curve cycles with minima given by the "x" symbol. Bottom panel: thickness estimation plotted against time.

A.3. Gaussian Fit

This appendix will explain the computational procedure to calculate the peak areas using Gaussian distributions. This will be done for an ice deposited at 10 K, 2×10^{-7} mbar and composing of $1H_2O$:$0.04CO_2$. The same steps are followed for other temperatures, deposition pressures and compositions. In every experiment, the window needs to be substracted to account for variations in the IR source from day to day and compensation of atmospheric H_2O and CO_2 interfering with the IR beam before it reaches the IR detector. The resulting absorbance spectra is plotted as a function of wavenumber ranging from 2365 to 2330 cm^{-1} (red dots in Figure A.7). To deconvolute the data, Gaussian functions are used in the following form:

$$g(x) = a\frac{1}{\sigma\sqrt{2\pi}}\exp\left(-\frac{1}{2}\frac{(x-\mu)^2}{\sigma^2}\right) \tag{A.7}$$

with a the amplitude, μ the expected peak center and σ being the standard deviation. In total, three Gaussians are worked with resulting (for mixtures) in a total of nine parameters (six for two Gaussians in pure CO_2 ice). A range of values is attributed to the nine parameters and the fitting uses the scipy.optimize.curve.fit tool in Python. The peak location of the orange Gaussian is fixed, being 2345 cm^{-1} at 10 K which is the same as for a pure CO_2 ice. The other parameters have lower and upper bound limits for amplitude and σ. Ultimately, the three Gaussian distributions are fitted using the trapezoidal rule. The plot in Figure A.7 visualizes the result of the fitting process together with the original data. Three Gaussians can be distinguished, a blue one peaking at 2351 cm^{-1}, an orange area peaking at 2345 cm^{-1} and a green one at 2341 cm^{-1}. The lower panel visualizes the residual as a function of wavenumber. The residual is the portion of the data that is left over, or resides, after fitting the data. In other words, the portion of the data that was not fit. The spectrum and Gaussian distributions for a 25% CO_2 in water ice and pure CO_2 ice can be found in Figure A.8 and Figure A.9, respectively. Note that for both cases, the residuals at the beginning and end are generally higher than at other wavenumbers. This is due to the subtraction of the reference spectrum which does not always result in the spectrum starting and ending at 0 absorbance.

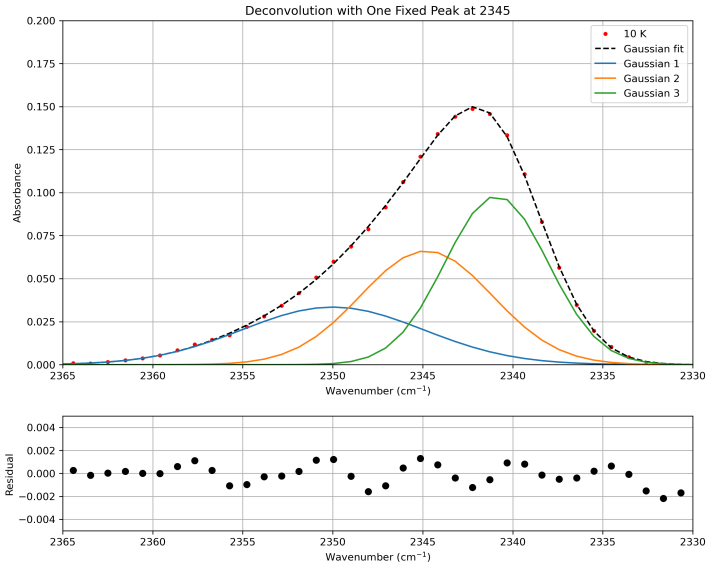

Figure A.7: Top panel: the red dots represent the experimental data for an ice deposited at 10 K and 2×10^{-7} mbar. The ice composition is $1H_2O$:$0.04CO_2$. The black dotted line is the Gaussian fit which splits into three separate Gaussian distributions: blue area peaking at 2351 cm^{-1}, the orange at 2345 cm^{-1} and the green at 2341 cm^{-1}. Lower panel: residual plotted as a function of wavenumber.

A.3.1. Error Estimate

Scientific analysis often involves fitting mathematical models to experimental data. In the case of Gaussian distributions, curve fitting aims to determine parameters like amplitude, mean (μ), and standard deviation (σ) for each Gaussian peak. After fitting, the covariance matrix provides the errors associated

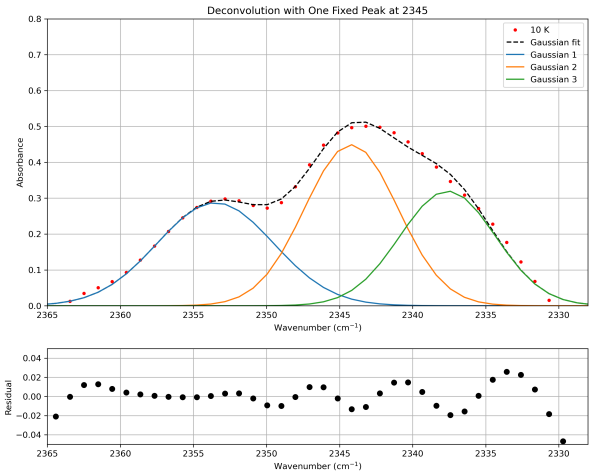

Figure A.8: Top panel: the red dots represent the experimental data for an ice deposited at 10 K and 2×10^{-7} mbar. The ice composition is $1H_2O$:$0.25CO_2$. The black dotted line is the Gaussian fit which splits into three separate Gaussian distributions: blue area peaking at 2353 cm^{-1}, the orange at 2345 cm^{-1} and the green at 2337 cm^{-1}. Lower panel: residual plotted as a function of wavenumber.

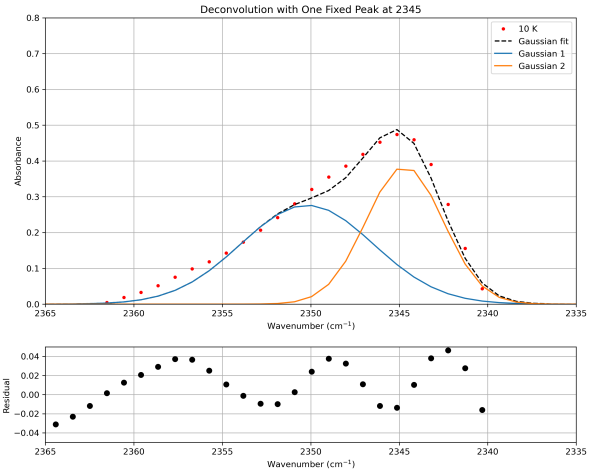

Figure A.9: Top panel: the red dots represent the experimental data for a pure CO_2 ice deposited at 10 K and 2×10^{-7} mbar. The black dotted line is the Gaussian fit which splits into two separate Gaussian distributions: blue area peaking at 2351 cm^{-1} and the orange at 2345 cm^{-1}. Lower panel: residual plotted as a function of wavenumber.

with these parameters. The integral of a Gaussian distribution represents the area under its curve and is often estimated using numerical methods like the trapezoidal rule. The uncertainty in this integral can be assessed through error propagation. The general formula for a Gaussian distribution is given by Equation A.7. When estimating the integral of a Gaussian function using the trapezoidal rule, the errors (δA) in this integral due to errors in the mean ($\delta\mu$) and standard deviation ($\delta\sigma$) can be computed via error propagation:

$$\delta A = \sqrt{(\frac{\delta A}{\delta \mu} \cdot \delta\mu)^2 + (\frac{\delta A}{\delta \sigma} \cdot \delta\sigma)^2} \tag{A.8}$$

Where:

- A represents the integral of the Gaussian distribution.
- $\frac{\delta A}{\delta \mu}$ and $\frac{\delta A}{\delta \sigma}$ are the partial derivatives of the integral with respect to the mean and standard deviation, respectively.

For the three Gaussian distributions model, the integrals (A_1, A_2, A_3) and their associated errors (δA_1, δA_2, δA_3) can be determined. Error propagation considers the partial derivatives of each integral with respect to the mean and standard deviation of each Gaussian peak, coupled with the errors from the fitted parameters, to compute the uncertainty in the integrals. The results are depicted in Figure A.10 for a low CO_2 concentration and Figure A.11 for a high concentration, respectively. These figure show the integrated absorbance area as a function of temperature for the three Gaussian distribution mentioned earlier. The errors are indicated by means of error bars, which are introduced in the figures. It must be noted that this method is used as a first estimate. The error is very sensitive to the values for the standard deviation, as these are taken for the pure CO_2 case. These impose a larger error than expected, as can also be seen when looking at the error bars in Figure A.10 and Figure A.11. Furthermore, the trapezoidal rule introduces its own numerical errors, and these errors can propagate through the calculations. It is advised for future work to included a more accurate method. However, this method still gives some insight in the behaviour of the integrated absorbance areas as a function of temperature.

A.4. DFT Simulation

To study the influence of porosity in amorphous CO_2, simulations were carried out using Density Functional Theory (DFT) (Hohenberg and Kohn 1964; Kohn and Sham 1965) and the CASTEP program

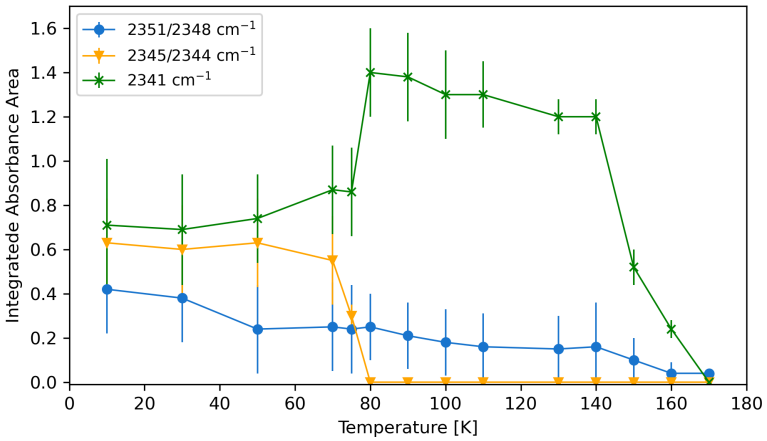

Figure A.10: Integrated absorbance areas of the three Gaussian distributions as a function of temperature for a $1H_2O$:$0.04CO_2$ layered ice. The error bars are indicated by vertical lines.

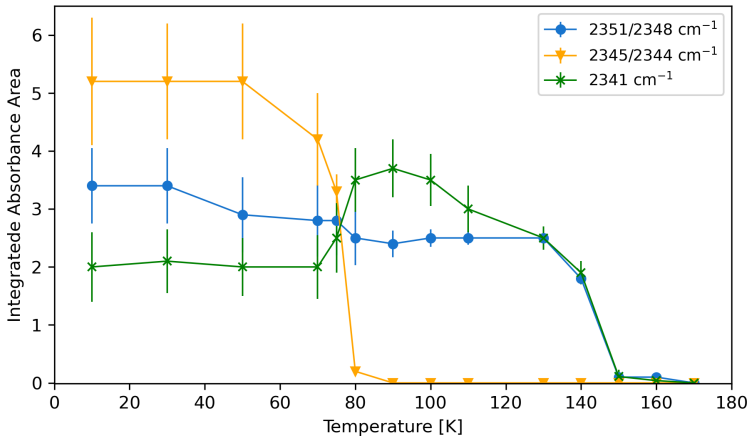

Figure A.11: Integrated absorbance areas of the three Gaussian distributions as a function of temperature for a $1H_2O$:$0.25CO_2$ layered ice. The error bars are indicated by vertical lines.

(Clark et al. 2005) for shape optimization and vibrational spectrum prediction.

Starting with a CO_2 crystal, the amorphous ice models are created by adding temperature using molecular dynamics (MD) until the structure melts. This was done with the Andersen barostat (Andersen 1980) at constant pressure and the Nose thermostat (Martyna et al. 1992) at rising temperatures. The porous model is then formed by removing CO_2 molecules from the amorphous model's core. DFT was then used to geometrically optimize the systems using the Generalized Gradient Approximation (GGA) and functionals by Perdew-Burke-Ernzerhof (PBE). Infrared spectra were simulated using density functional perturbation theory (Refson et al. 2006) based on these improved models. The calculated spectra are not intended to perfectly duplicate the measured wavenumbers for vibrational bands, but should be near within a margin of error. Most significantly, they are repeatable and can aid in understanding the influence of experimentally uncontrollable factors.

The spectra of an amorphous CO_2 model in blue and a porous CO_2 model in red are shown in Figure A.12. The chemical structure of the amorphous system is displayed on the left side of the two spectra, while the chemical structure of the porous system is depicted on the right. This clearly displays the difference between the two models, since CO_2 molecules are removed from the amorphous

core in the porous model. Starting with the amorphous model, the spectrum has the highest intensity around 2325 cm^{-1}, with a shoulder on the blue peaking around 2340 cm^{-1}. If compared with the porous CO_2 model, a clear shift to the blue is seen to 2336 cm^{-1}. This also holds for the shoulder, which has now a very clear peak around 2350 cm^{-1}. This simulation shows the effect of porosity on the CO_2 asymmetric stretching band, resulting in a blue shift of both peaks. Is must be stressed that the goal of this simulation is to simulate the effect of porosity on the peak location and therefore finding the mechanism behind the shift rather than matching perfectly the peak location with the same wavenumbers.

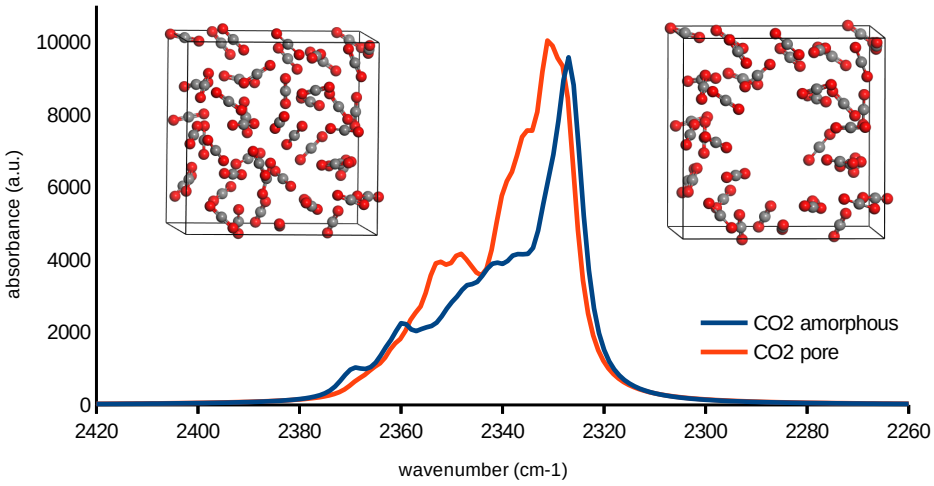

Figure A.12: DFT spectra for amorphous CO_2 (blue) and CO_2 in a pore (red) as a function of wavenumber.

A.5. JWST Observations

Before analyzing laboratory spectra to JWST observations, the relevant data has to be retrieved and calibrated. This is done by using the base code of another MSc student with my additions. The JWST data retrieval will be discussed first in subsection A.5.1. The process of plotting the latitudes and longitude of Ganymede's leading hemisphere is discussed in subsection A.5.2 and subsection A.5.3, respectively.

A.5.1. Data Retrieval

The JWST data is open source and accessible through the Mikulski Archive for Space Telescopes (MAST) platform. All Jovian system observations, including NIRSpec and MIRI observations, may be found using proposal ID 1373. The needed data may then be downloaded in the form of Flexible Image Transport System (FITS) files, which are a popular astronomical format. The observation recorded in the FITS file may be deduced from the file's name. jw01373019001_03101_00001_nrs1_uncal.fits, for example, is a JWST observation of proposal 1373. It bears observation number 19, indicating that it comes from Ganymede's leading hemisphere. This is dither 1 of the four dithers, and the detector is nrs1.

After downloading the necessary FITS files, they may be imported into a Python environment. To access the data, one must first understand how the data is stored. Data cubes are present in every FITS file. The flux values for all NIRSpec's IFU pixels are known for each detected wavelength. The average flux at each wavelength is calculated over Ganymede's disk in order to construct a spectrum. Bad pixels are cleaned away throughout this procedure. The standard deviation of all flux measurements at a given wavelength may be calculated using the z-score. Outliers (standard deviations greater than 4) will be ignored in this case. An example of a resulting flux spectrum of the leading hemisphere is shown in Figure A.13. The image clearly shows the existence of Solar lines, which will be filtered away in order to determine Ganymede's characteristics.

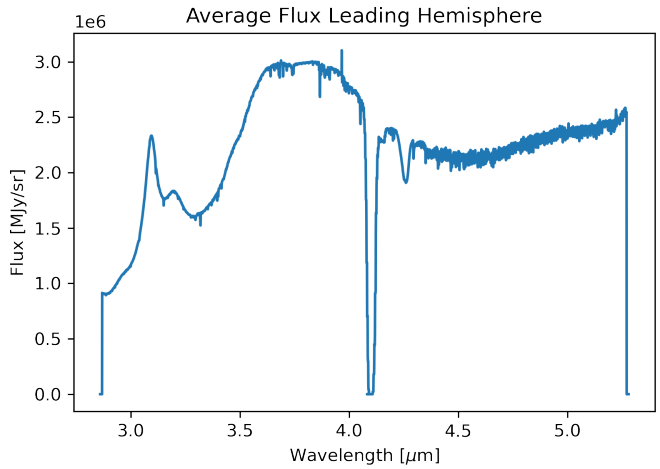

Figure A.13: Flux spectrum of the leading hemisphere of Ganymede.

When Ganymede's received flux is determined, it is critical to appropriately filter out the Solar lines in order to thoroughly analyze Ganymede's characteristics. Because the accessible Solar spectrum is in a Solar inertial reference frame, a Doppler shift must be considered before dividing the received flux by the Solar spectrum. Light from the Sun is reflected on Ganymede before being detected by the JWST. The end results can be seen in Figure A.14 which shows the I/F (observed intensity divided by the incident flux) as a function of wavelength. Note the gap between 4 and 4.15 μm. Because the signal is caught by two detectors in the NIRSpec instrument, nrs1 and nrs2, this is the case. There is a physical gap between these two detectors that eliminates the 4 - 4.15 μm region from the spectra.

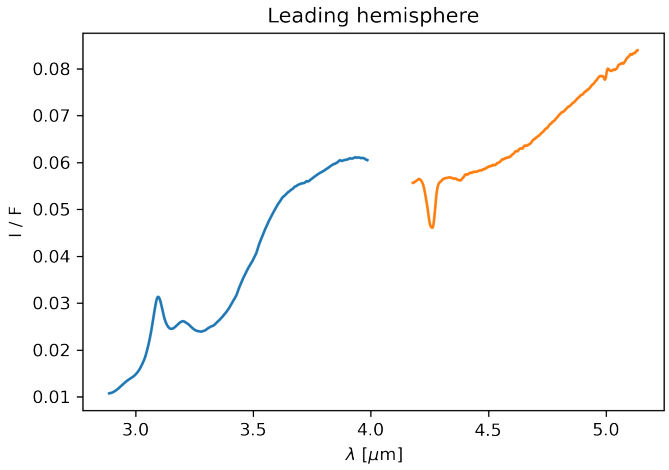

Figure A.14: Spectrum of Ganymede's leading hemisphere after calibrating for the solar flux.

A.5.2. Latitudes

Before the latitudes can be plotted, necessary variables and reading the spectral data from JWST files for two different detectors (NRS1 and NRS2) are done. Wavelength grids are calculated for both detectors based on the header information of the spectral data. The flux data is processed through an iterative loop, accounting for spatial coordinates and data validity checks. Outlier detection, filtering, and averaging steps are applied to ensure robust and meaningful flux values. Next, a velocity correction is applied to convert the observed wavelength to Webb wavelength, providing a more accurate representation of the spectral information. The solar irradiance data (calculated in previous step) is read from external files, providing a reference for normalization and further analysis. The I/F (Intensity

to Flux) ratio is calculated by dividing the processed flux values by the corresponding solar irradiance values, facilitating a normalized comparison. The result if this procedure is visualized in Figure A.15. Data relevant to CO_2 absorption features is selectively extracted based on a specified wavelength range, preparing it for visualization.

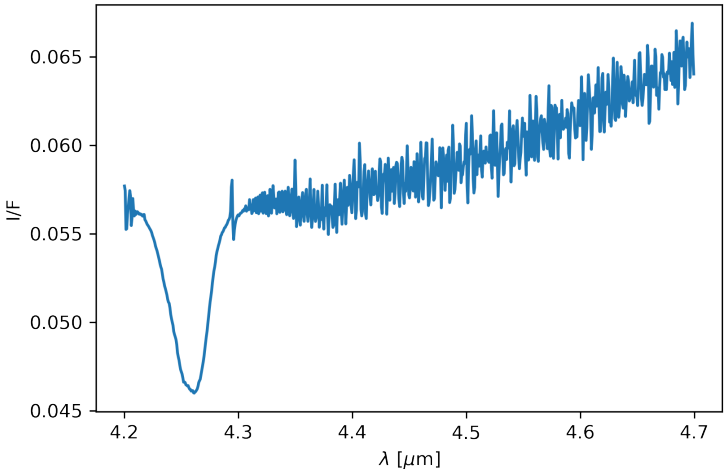

Figure A.15: I/F plotted as a function of wavelength between the range of 4.2 μm and 4.7 μm to highlight the CO_2 absorption features.

For the analysis of the latitudes, specific data points corresponding to the wavelength range of interest (4.2 to 4.315 micrometers) are extracted and is associated with the analysis of CO_2 features. The latitudes are divided into ranges of 30 degrees, for example from 0 to 30 degrees North. For each wavelength falling within a specific range (4.2 to 4.315 μm), the code processes pixel data from a 2D array. Within this pixel data, certain conditions, like latitude range are checked, and if met, the corresponding flux values are appended to a flux list of pixels. Outliers are filtered out, the list is ordered in descending order and the average of its non-zero values is computed. This is then appended to the flux values for that specific range of latitudes. The flux values need to be re-scaled to create relative fluxes for the different latitude ranges. The ratio of flux values to solar irradiance is calculated next for different latitudes. The results of this procedure for different latitude ranges are given in Figure A.16.

A.5.3. Longitudes

The same process to calculate the longitudes is applied as for latitude calculations. It is important to mention that the files that are worked with are East oriented. This is transformed to West degrees for a better appreciation of the morning and evening limb. The longitudes are calculated between 60 degrees North and 60 degrees South. The results are shown in Figure A.17.

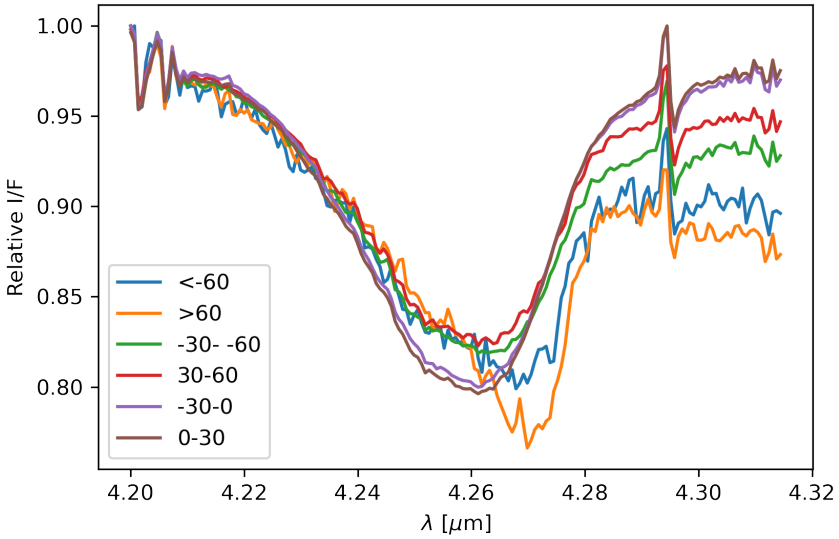

Figure A.16: Relative I/F plotted as a function of wavelength for different latitude ranges.

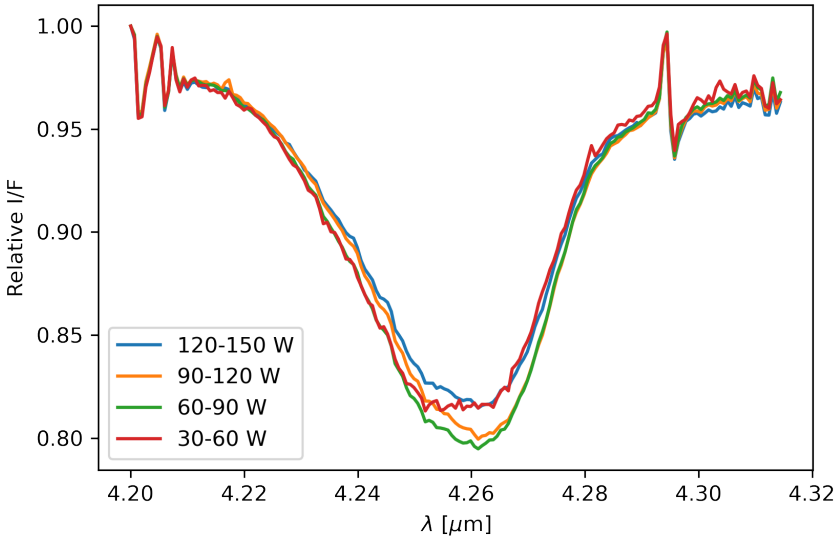

Figure A.17: Relative I/F plotted as a function of wavelength for different longitudinal ranges.

B

Additional Experiments

During the timeframe in Madrid, various experiments were conducted. However, due to the considerable time required for a thorough analysis, the results from these experiments were not incorporated into the paper presented in this project. Furthermore, some of these experiments would have significantly diverged from the primary focus, potentially causing distraction and confusion for the reader. Nevertheless, these outcomes, believed to be promising and capable of prompting significant studies, are included here. The emphasis is placed on facilitating the reproducibility of these experiments.

B.1. CO_2 Abundance in Water Ice

CO_2/H_2O mixtures reveal an outstanding behaviour and have a strong effect on the CO_2 band profiles, which is of extreme importance for the abundance determinations and studies of interstellar CO_2. When the amount of water ice in a CO_2/H_2O ice mixture exceeds a few percent, additional trapping sites are formed which lead to a very peculiar profile of the CO_2 stretching mode (Ehrenfreund 1997b). In Figure B.1, it is shown that a second band appears at 2330 cm^{-1}, which results in an enormous broadening of the band and an asymmetric profile which is shifted by about 12 cm^{-1} to lower frequency. This second band becomes broader to equal concentrations of H_2O and CO_2. In polar mixtures, where the H_2O is more abundant in the ice matrix, the band position peak again around 2341 cm^{-1}, closer to that of pure CO_2. Also the width of the peak is reduced again.

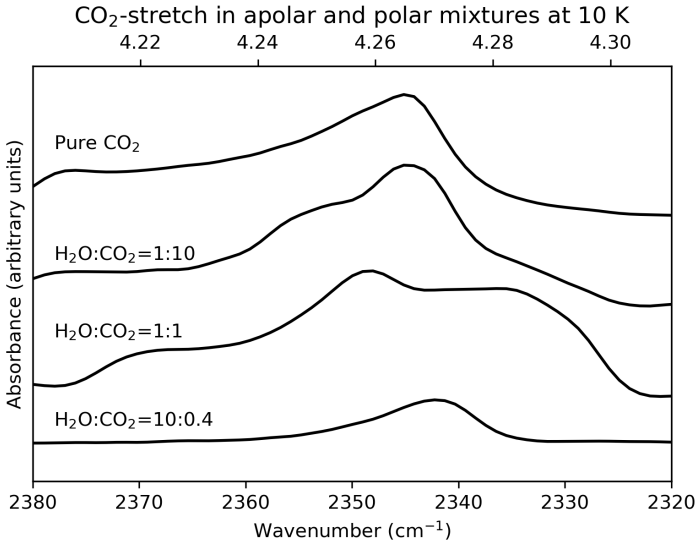

Figure B.1: Infrared spectra of the solid CO_2 stretching mode in CO_2/H_2O mixtures. A peculiar profile is observed for the CO_2 stretch, which is shifted to lower frequencies and characterized by a large band width.

B.2. Higher Deposition Pressure and Temperature

Experiment were carried out with a higher deposition temperature, namely 70 K, to show the effect temperature has on the CO_2 stretching band. Additionally, a higher deposition pressure is also analyzed. The most relevant experiments are listed below:

1. 10 K, 8e-7 mbar, $1H_2O$:$0.04CO_2$
2. 10 K, 8e-7 mbar, $1H_2O$:$0.1CO_2$
3. 70 K, 2e-7 mbar, $1H_2O$:$0.04CO_2$
4. 70 K, 2e-7 mbar, $1H_2O$:$0.25CO_2$

From the above experiments, the spectra as a function of temperature will be given together with the QMS data. All ices are warmed up with a heating rate of 0.2 K/min unless stated otherwise.

First, the effect of deposition pressure is analyzed. The spectra for a H_2O/CO_2=1:0.04 ice mixture deposited at 10 K and 8e-7 mbar are given in Figure B.2 and the TPD curve is visualized in Figure B.3. The spectra for a 10 K deposited H_2O/CO_2=1:0.1 ice mixture at 8e-7 mbar are visualized in Figure B.4. The TPD curve is plotted in Figure B.5. Looking at the spectrum of 10 K in Figure B.2, it is observed that the shoulder shifted to the blue compared to the lower deposition pressure. As mentioned in the paper, a higher deposition pressure changes the ice to a more porous state with as result shifting the shoulder to the blue. The same is true for the 10 K spectrum of Figure B.4. As for the TPD curves, Figure B.3 shows three distinct desorption peaks, namely around 80 K, 145 K and the final one around 160 K. The same is true when looking at Figure B.5. However, a warm-up rate of 1 K/min is now applied with the first peak around 85 K, the second around 150 K and the final one at 175 K. This means that the higher warm-up rate delays the deosorption of the carbon dioxide and water molecules by just a few Kelvin.

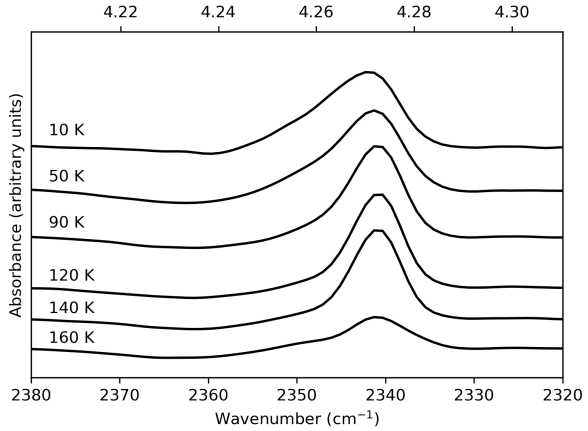

Figure B.2: Infrared absorption spectra of the stretching mode of solid CO_2 in a H_2O/CO_2=1:0.04 mixture during warm-up. The ice is deposited with a pressure of 8e-7 mbar.

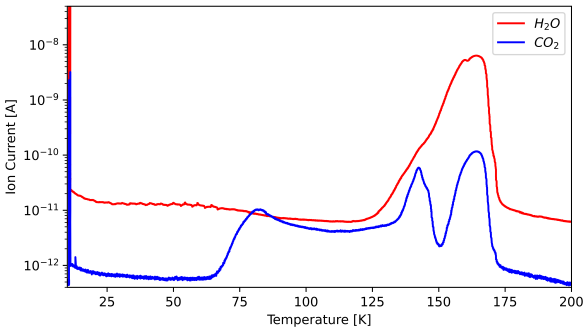

Figure B.3: TPD curve of a H_2O/CO_2=1:0.04 ice mixture.

The effect of deposition temperature on the CO_2 stretching band is now discussed by analyzing two additional experiments. These ices are deposited with a temperature of 70 K. The spectra of a H_2O/CO_2=1:0.04 mixture deposited at 70 K and 2e-7 mbar are given by Figure B.6. The TPD curve is plotted in Figure B.7. The spectrum at 70 K in Figure B.6 doesn't seem to be different from the spectrum at the same temperature deposited at 10 K. The same holds for the TPD curve, where again three desorption peaks are visible. The spectra of a H_2O/CO_2=1:0.25 mixture desposited at 70 K and 2e-7 mbar are given by Figure B.8. Below 90 K, the same band profile can be identifies as before where the spectrum can be deconvoluted into three Gaussian distributions. Above 85 K, something peculiar happens when looking at the TPD curve in Figure B.9. When comparing the TPD curve to the spectrum, it seems that at 85 K the pure CO_2 thermally desorbs and right after at around 100 K the a vast majority of the shoulder peaking at 2352 cm^{-1} desorbs.

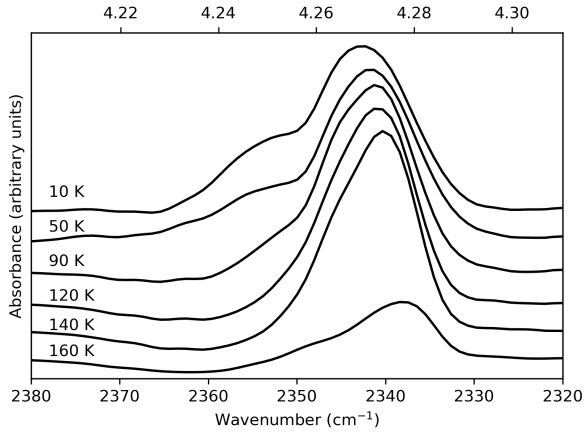

Figure B.4: Infrared absorption spectra of the stretching mode of solid CO_2 in a H_2O/CO_2=1:0.1 mixture during a warm-up of 1 K/min. The ice is deposited with a pressure of 8e-7 mbar.

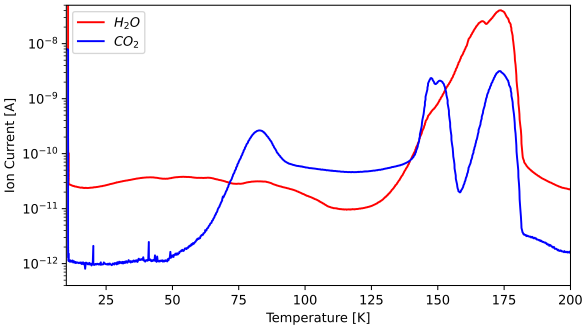

Figure B.5: TPD curve of a H_2O/CO_2=1:0.1 ice mixture.

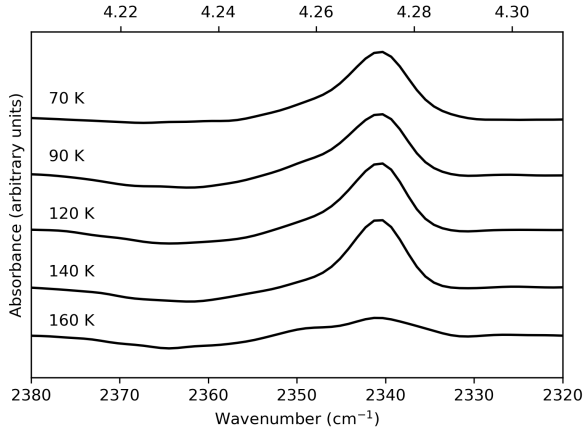

Figure B.6: Infrared absorption spectra of the stretching mode of solid CO_2 in a H_2O/CO_2=1:0.04 mixture during warm-up. The ice is deposited with a pressure of 2e-7 mbar and a temperature of 70 K.

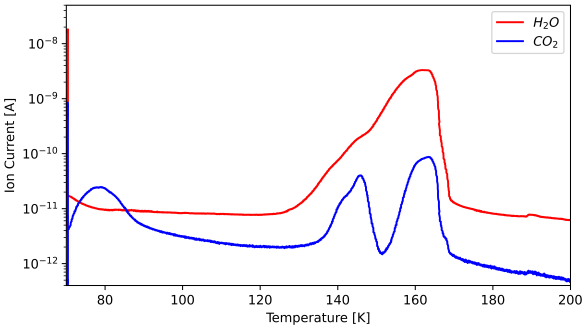

Figure B.7: TPD curve of a H_2O/CO_2=1:0.04 ice mixture deposited at 70 K and 2e-7 mbar.

B.3. UV irradiation

The surfaces of celestial icy bodies within the Solar System endure constant exposure to charged particles emitted by the solar wind or planetary magnetospheres. Moons adorned with ice, orbiting massive gas giants, present an intriguing alternative to Earth-like planets in the quest for life beyond our planet. The notable quantity of Jupiter-sized exoplanets discovered to date, coupled with the prevalence of water in space, renders these environments particularly compelling for exploration. The external onslaught of UV and X-rays, cosmic rays, as well as energetic electrons onto these frozen surfaces can potentially alter the composition and physical structure of the ice. These modifications may have chemical implications that affect the formation of intricate organic compounds (Muñoz Caro et al. 2019). Consequently, it becomes crucial to comprehensively comprehend the impact of various weathering agents on these surfaces. For this reason, one experiment was carried out where a H_2O:CO_2= 2.2:1 ice was irradiated with a UV lamp for 120 minutes. The ice is deposited at 70 K and at a pressure of 8×10^{-7} mbar. The same procedure is maintained for the deposition of the ice. Once the ice is deposited, the window with the deposited ice is faced to the UV lamp. Note that the UV lamp needs to warm up before it can be used. In Table B.1, the time, photon dose and cycle are given for reproducibility. As shown in Figure B.10, the deposited ice at 70 K is peaking at 2346 cm^{-1}. After 15 minutes of irradiation, the peak shifts to the blue and this stay up to an irradiation time of 60 minutes. After, the peak location shifts back to the original peak location as is illustrated with the green graph.

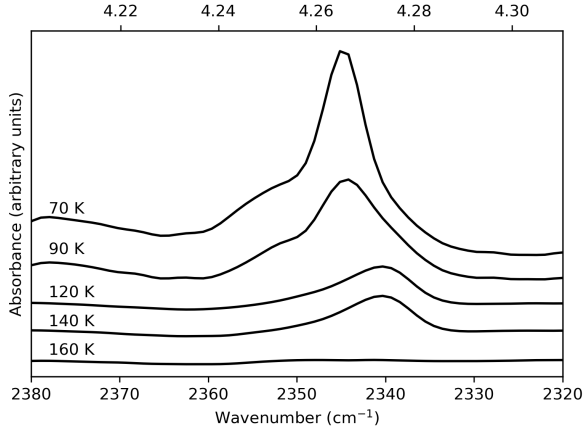

Figure B.8: Infrared absorption spectra of the stretching mode of solid CO_2 in a H_2O/CO_2=1:0.25 mixture during a warm-up of 0.5 K/min. The ice is deposited with a pressure of 2e-7 mbar and a temperature of 70 K.

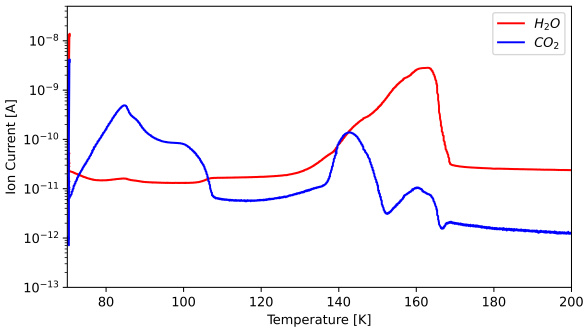

Figure B.9: TPD curve of a H_2O/CO_2=1:0.25 ice mixture deposited at 70 K and 2e-7 mbar.

Table B.1: Experimental parameters for an ice that is UV irradiated for 120 minutes.

Time	Acc. Time (min)	Photon Dose (photons cm^{-1}s^{-1})	Cycle
0	-	4.735e^{16}	-
15	15	7.865e^{16}	665-751
15	30	1.119e^{17}	805-893
30	60	1.803e^{17}	990-1167
60	120	3.281e^{17}	1367-1721

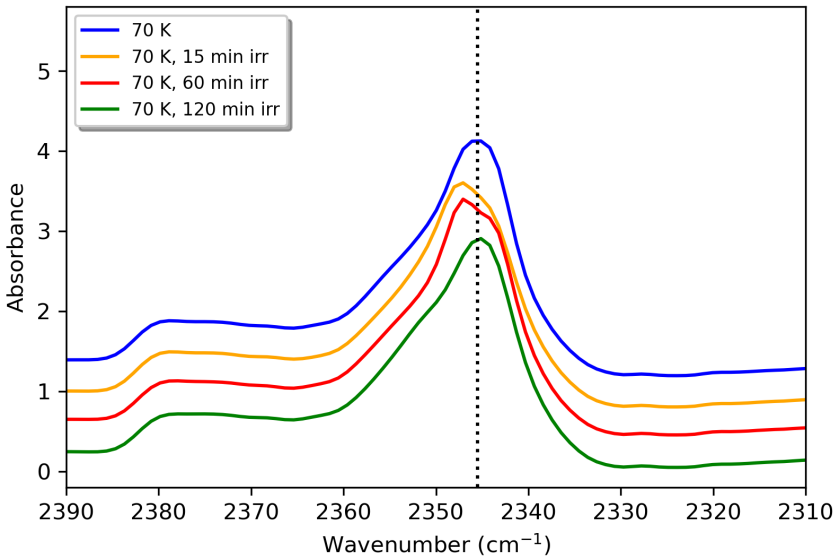

Figure B.10: The effect of radiation on the CO_2 band at 2345 cm^{-1}. The ice is deposited at 70 K and irradiated for 120 minutes in total. A spectrum is taken after 15 minutes, 60 minutes and 120 minutes. The dotted line is located at 2346 cm^{-1}.

References

Andersen, H. C. (1980). “Molecular dynamics simulations at constant pressure and/or temperature.” In: *J. Chem. Phys.* 71, p. 2384.

Bernstein, M.P. et al. (2005). “Near-infrared laboratory spectra of solid H2O/CO2 and CH3OH/CO2 ice mixtures.” In: *Icarus* 179, pp. 527–534.

Bockelée-Morvan, D. et al. (2023). “Composition and thermal properties of Ganymede’s surface from JWST/NIRSpec and MIRI observations”. In: *Astron. Astrophys.*

Buratti B.J., et al. (2005). “Cassini visual and infrared mapping spectrometer observations of Iapetus: Detection of CO2”. In: *Astrophys. J.* 622 (2), pp. L149–L152.

Carr, M. H. et al. (1998). “Evidence for a subsurface ocean on Europa”. In: *Nature* 391.363-365.

Clark, S. J. et al. (2005). “First principles methods using CASTEP”. In: *Z. Kristall.* 220, pp. 567–570.

Crovisier, J. (2006b). “New trends in cometary chemistry.” In: *Faraday Discuss.* 133, pp. 375–385.

— (2006a). “Recent results and future prospects for the spectroscopy of comets.” In: *Mol. Phys.* 104 (16–17), pp. 2737–2751.

Dartois, E. et al. (2005). “Spitzer’s large CO2 ice detection toward the L723 class 0 object”. In: *Astron. Astrophys.* 444, pp. L57–L60.

Draine, B.T. (2003). “Interstellar dust grains.” In: *Annu. Rev. Astron. Astrophys.* 41, pp. 241–289.

Ehrenfreund, P. et al. (1997b). “In preperation for J. Chem. Phys.” In.

Gerakines, P. A. et al. (1995). “The infrared band stregths of H_2O, CO and CO_2 in laboratory simulations of strophysical ice mixtures.” In: *Astronomy and Astrophysics* 296.

González Díaz, C. et al. (2022). “Density and infrared band strength of interstellar carbon monoxide (CO) ice analogues”. In: *MNRAS* 517, pp. 5744–5755.

Grundy, W.M. et al. (2003). “Discovery of CO2 ice and leading–trailing spectral asymmetry on the uranian satellite Ariel”. In: *Icarus* 162, pp. 222–229.

Hohenberg, P. and W. Kohn (1964). “Inhomogeneous electron gas”. In: *Phys. Rev.* 136, B864–B871.

Kohn, W. and L. J. Sham (1965). “Self-consistent equations including exchange and correlation effects”. In: *Phys. Rev.* 140, A1133–A1138.

Kumi, G. et al. (2006). “Amorphous solid water films: Transport and guest–host interactions with CO2 and N2O dopants.” In: *J. Phys. Chem.* A 110, pp. 2097–2105.

Malyk, S. et al. (2007). “Trapping and release of CO2 guest molecules by amorphous ice.” In: *J. Phys. Chem.* A 111, pp. 13365–13370.

Martyna, G. L. et al. (1992). “Nosé-Hoover chains: The canonical ensemble via continuous dynamics”. In: *J. Chem. Phys.* 97, pp. 2635–2645.

Muñoz Caro, G. M. et al. (2019). “X-ray versus UV irradiation of astrophysical ice analogs leading to COMs formation.” In: *ACS Earth and Space Chemistry, invited article to Special Issue entitled Complex Organic Molecules (COMs) in Star-Forming Regions* 3, pp. 2138–2157.

Refson, K. et al. (2006). “Variational density-functional perturbation theory for dielectrics and lattice dynamics”. In: *Phys. Rev. B* 73, p. 155114.

Sandford, S.A. and L.J. Allamandola (1990). “The physical and infrared spectral properties of CO2 in astrophysical ice analogs.” In: *Astrophys. J.* 355, pp. 357–370.

Spencer, J.R. et al. (1999). “Temperatures on europa from galileo photopolarimeter-radiometer: night-time thermal anomalies”. In: *Science* 284, pp. 1514–1516.

Trumbo, S.K. et al. (2019). “H_2O_2 within Chaos Terrain on Europa’s Leading Hemisphere”. In: *The Astronomical Journal* 158, p. 127.

Trumbo, S.K. et al. (2023). “Hydrogen Peroxide at the poles of Ganymede”. In: *Science Advances* 9, eadg3724.

Villanueva, G. L. et al. (2023). “Endogenous CO2 ice mixture on the surface of Europa and no detection of plume activity”. In: *Science* 381, pp. 1305–1308.